ORNL/TM-2023/3078

Microstructural Characterizations of Two High Fluence Baffle-Former Bolts Retrieved from a Westinghouse Two-loop Downflow Type PWR

Timothy G. Lach
Maxim N. Gussev
Xiang (Frank) Chen

September 2023

OAK RIDGE National Laboratory

ORNL IS MANAGED BY UT-BATTELLE LLC FOR THE US DEPARTMENT OF ENERGY

ORNL/TM-2023/3078

Light Water Reactor Sustainability (LWRS) Program
Materials Research Pathway
M3LW-23OR0402055

MICROSTRUCTURAL CHARACTERIZATIONS OF TWO HIGH FLUENCE BAFFLE-FORMER BOLTS RETRIEVED FROM A WESTINGHOUSE TWO-LOOP DOWNFLOW TYPE PWR

Timothy G. Lach[1], Maxim N. Gussev[2], Xiang (Frank) Chen[1]

[1]Materials Science and Technology Division
[2]Nuclear Energy and Fuel Cycle Division
Oak Ridge National Laboratory

September 2023

Prepared by
OAK RIDGE NATIONAL LABORATORY
Oak Ridge, TN 37831-6136
managed by
UT-BATTELLE LLC
for the
US DEPARTMENT OF ENERGY
under contract DE-AC05-00OR22725

This page intentionally left blank

CONTENTS

LIST OF FIGURES

LIST OF TABLES

This page intentionally left blank

ACKNOWLEDGEMENTS

This research was sponsored by the U.S. Department of Energy, Office of Nuclear Energy, Light Water Reactor Sustainability Program, Materials Research Pathway, under contract DE-AC05-00OR22725 with UT-Battelle, LLC/Oak Ridge National Laboratory (ORNL).

Atom probe tomography (APT) research was conducted as part of a user project at the Center for Nanophase Materials Sciences (CNMS), which is a US Department of Energy, Office of Science User Facility at Oak Ridge National Laboratory. We would like to thank Jonathan Poplawsky and James Burns for help with APT data collection

The authors extend their appreciation to Clay Morris, Jerid Metcalf, Mark Delph, and other colleagues at Irradiated Materials Examination and Testing Facility (IMET) at ORNL for their support of sample processing during the hot cell sample retrieval. In addition, we would like to thank Patricia Tedder and Travis Dixon at the Low Activation Materials Development and Analysis (LAMDA) laboratory at ORNL for receiving, cleaning, inventorying, and polishing the irradiated samples. Lastly, we would like to thank the late Mike Burke formerly with Electrical Power Research Institute who was involved in the bolt havesting and characterization planning and led the sample preparation, machining, and shipping when he was working at Westinghouse Electric Company.

This page intentionally left blank

EXECUTIVE SUMMARY

As one of the pressurized water reactor (PWR) internal components, baffle-former bolts (BFBs) are subjected to significant mechanical stress and neutron irradiation from the reactor core during the plant operation. Over the long operation period, these conditions lead to potential degradation and reduced load-carrying capacity of the bolts. In support of evaluating long-term operational performance of materials used in core internal components, the Oak Ridge National Laboratory (ORNL), through the Department of Energy (DOE), Office of Nuclear Energy, Light Water Reactor Sustainability (LWRS) Program, Materials Research Pathway (MRP), has harvested two high fluence BFBs from a commercial Westinghouse two-loop downflow type PWR. The two bolts of interest, i.e. bolts # 4412 and 4416, were withdrawn from service in 2011 as part of a preventative replacement plan. No identification of cracking or potential damage was found for these bolts during their removal in 2011. However, the bolts required a lower torque for removal from the baffle structure than the original torque specified during installation. Irradiation damage levels in the bolts range from 15 to 41 displacements per atom. The goal of this project is to perform detailed microstructural and mechanical property characterization of BFBs following in-service exposures. The information from these bolts will be integral to the LWRS program initiatives in evaluating end of life microstructure and properties. Furthermore, valuable data will be obtained that can be incorporated into model predictions of long-term irradiation behavior and compared to results obtained from experimental reactor conditions.

In this report, we present our latest study in FY23 on microstructural characterizations of both baffle-former bolts using atom probe tomography characterization to understand the degree of radiation-induced precipitation and segregation and using analytical scanning electron microscopy on BFB #4412 to reveal the formation of irradiation-assisted stress corrosion cracking at the surface. The radiation-induced defects in the material add to the large wealth of knowledge for neutron-induced defects in 304/316 grades of stainless steels, specifically for radiation-induced precipitation after high fluence commercial PWR irradiation. The main findings are summarized as follows:

1) Radiation-induced precipitation in the the two BFBs was highly complex, with the volume fraction and size of Ni/Si and Cu-rich precipitates depending strongly on the radiation temperature/dose. Comparing the two bolts, clustering was essentially the same for both bolts in the CS or bolt head section, but Ni/Si clustering was much higher in the BS or bolt thread section in the high dose bolt #4412 than in the lower dose bolt #4416.
2) Solute segregation out of solution was highest for most solute elements in the thread section of both bolts with the exception of Cu, which experienced more separation out of solution into Cu-rich clusters in the bolt head section. Solute segregation of each element out of solution was also more pronounced in the higher dose bolt #4412 than in the lower dose bolt #4416 in the BS and MS (middle shank) sections.
3) The lack of much change in solute segregation out of solution in the head section between the two bolts suggests that a steady-state for structural evolution has been reached in the CS section by the dose in the CS section of the lower dose bolt #4416. Gradients in temperature, strain, and neutron energy not only affect the steady-state size and distribution of precipitates but also the kinetics of when the steady-state is reached. The lower temperature of the CS section of the BFB reaches its steady-state sooner than the higher temperature of the MS and BS sections, which also have larger precipitate sizes.
4) SEM characterization of the intersection of the bolt head with the bolt shank of the higher dose bolt #4412, where the bolt was exposed to primary coolant water, reveals microcracks formed only in regions where there was additional stress due to the curvature of the bolt suggesting that irradiation assisted stress corrosion cracking (IASCC) is a cause for these cracks. The cracks observed are short – <~6 μm long – and only travel along high angle grain boundaries.

This page intentionally left blank

1. INTRODUCTION

As one of the pressurized water reactor (PWR) internal components, baffle-former bolts (BFBs) are subjected to significant mechanical stress and neutron irradiation from the reactor core during the plant operation. Over the long operation period, these conditions lead to potential degradation and reduced load-carrying capacity of the bolts, and life extension of existing PWRs would only cause more damage to the bolt material. Indeed, the BFB has been a particular concern for the nuclear industry since the first observation of failed bolts following the investigation of flow-induced vibration of fuel rods in elements on the core periphery observed in French 900 MW plants in the 1980s [1]. In the United States, the first degraded BFBs were observed in 1999. In support of evaluating long-term operation performance of materials used in core internal components, the Materials Research Pathway (MRP) under the U.S. Department of Energy (DOE), Office of Nuclear Energy, Light Water Reactor Sustainability (LWRS) Program pursued the retrieval of aged structural components for the study of the microstructure, mechanical, and corrosion-related properties including stress corrosion cracking (SCC) and irradiation-assisted stress corrosion cracking (IASCC) initiation and growth. To this end, the MRP successfully harvested two high fluence BFBs from a Westinghouse two-loop downflow type PWR in 2016. In the same year, the two BFBs were received at the Westinghouse Churchill facility for inspection and specimen fabrication. The fabrication was completed in 2017 with specimens shipped to Oak Ridge National Laboratory (ORNL) for further testing.

In this report, we present our latest study in FY23 on microstructural characterizations of both high fluence baffle-former bolts. The objective of this project is to provide information that is integral to evaluating end of life microstructure and properties as a benchmark of international models developed for predicting radiation-induced swelling, segregation, precipitation, and mechanical property degradation. Initial characterizations in FY19 [2] and FY22 [3] focused on electron microscopy-based microstructural characterizations and microhardness testing for both harvested BFBs and atom probe tomography (APT) characterization of the higher dose bolt, i.e., bolt #4412. Fracture toughness and fatigue crack growth rate testing results of both BFBs have also been published in the FY21 milestone report [4] for this project. Those initial microstructural characterizations utilized transmission electron microscopy (TEM) and scanning TEM (STEM). Here, for comparison with the TEM and STEM results, APT was performed to determine elemental segregation mechanisms with high resolution on both bolts. Results from this study specifically fill the knowledge gaps for the mechanisms of radiation-induced precipitation as a function of radiation temperature and radiation dose for type 316 austenitic stainless steels used in commercial PWR power plants. Additionally, initial results are presented on the study of in-service IASCC via scanning electron microscopy (SEM)-electron backscatter diffraction (EBSD) and energy dispersive X-ray spectroscopy (EDS) imaging and mapping surface microcracks found at the intersection of the bolt head and bolt shank in the higher dose bolt which was exposed to primary coolant water [5].

2. EXPERIMENTAL

2.1 Materials

The two harvested BFBs had the highest fluence among bolts withdrawn from service in 2011. Both bolts showed no indication of cracking during the ultrasonic inspection and in visual inspection following removal from service. However, the bolts required a lower torque for removal from the baffle structure than the original torque specified during installation. Figure 2.1 shows images of the bolt heads of two retrieved BFBs; no indication of surface cracking was observed in the transition region between the shaft and head, although some surface debris scale flaked off from the bolt body. The shiny gray portion of the bolt head was due to electric discharge machining (EDM) when the bolts were removed from the baffle wall. However, both bolts do still have some of the original surface that was exposed to coolant water where the bolt head intersects with the bolt shank, as circled in Figure 2.1(b). The ID number for the bolts

follows a 4-digit code with the first number being the quadrant location in the reactor, then the associated baffle plate number, the column location of the bolt associated with the particular baffle plate number, and finally the former plate location where the bolt originated. The composition in both atomic percent (at%) and weight percent (wt%) for both bolts as determined by APT is presented in ***Table 2.1***. These bolts are within the specifications for type 316-SS with slightly elevated Cr content, but this could be due to local variations.

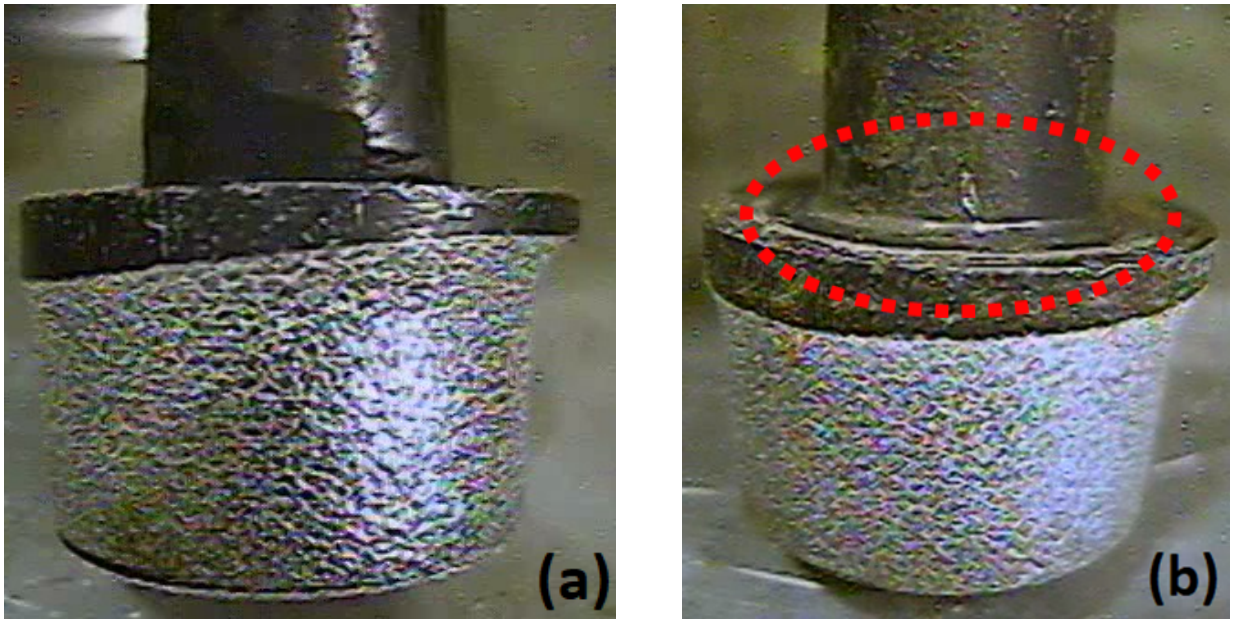

Figure 2.1*: Images of bolt heads for bolt #4412 in (a) and bolt #4416 in (b). Surface of bolt at bolt head/shank intersection (circled) was exposed to primary water and is still intact* [6]

Table 2.1*: Average compositions of bolt 4412 and 4416 from all of the APT reconstructions for each bolt in comparison with material specification (wt%) for 316 SS*

	BFB-4412		BFB-4416		316-SS Spec
Element	At%	Wt%	At%	Wt%	Wt%
Fe	64.19	64.62	64.56	64.96	Bal.
Ni	11.55	12.22	11.39	12.04	10.00-14.00
Cr	19.32	18.11	19.36	18.14	16.00-18.00
Mn	1.62	1.60	1.67	1.65	2.00 max
Mo	1.18	2.04	1.18	2.04	2.00-3.00
Si	1.24	0.63	1.15	0.58	1.00 max
C	0.20	0.043	0.19	0.040	0.08 max
P	0.024	0.013	0.027	0.015	0.040 max
Cu	0.26	0.29	0.25	0.28	0.75 max

Table 2.2 provides information on the range of fluences and estimated displacement damage along the length of the two bolts. The displacement damage values for the two bolts range from 15 to 41 displacements per atom (dpa) assuming a fluence to dpa conversion value of 6.7×10^{20} n/cm^2, E > 1 MeV per dpa [7]. Other important information for the two retrieved bolts not available at the time of preparation of this report includes the irradiation temperature profile, irradiation flux, and thermomechanical stress state. These require more complicated modeling and calculation and can vary within each power cycle and from cycle to cycle. For instance, calculations [8] from Point Beach Unit 2, which is another Westinghouse two-loop type PWR, showed that the irradiation temperature and flux for a BFB from a region next to the

bolt 4416 studied in this work varied in the range of 323-344 °C and 7.5×10^{12}-1.8×10^{13} n/cm^2-sec (E > 1 MeV) along the length of the bolt, respectively. Similarly, a baffle-former bolt removed from the Tihange 1 PWR showed a variation in irradiation temperature of about 23 °C (320-343 °C) along the bolt and a damage dose that was 2.6X higher in the bolt head (19.5 dpa) than the bolt thread (7.5 dpa) [9]. Therefore, the value for a detailed calculation on irradiation temperature and flux of BFBs may be limited due to the large variation of those parameters during the lifetime of a BFB. It is worth noting that Point Beach Unit 2 was originally a Westinghouse two-loop downflow type PWR but was converted to upflow in November 1986 [8].

***Table 2.2**: Fluence and estimated displacement damage distributions for two retrieved BFBs*

Bolt #	Fluence (10^{22} n/cm^2, E > 1 MeV)/Estimated dpa		
	Head	Mid-shank	Mid-thread
4412	2.78/41	2.27/34	1.46/22
4416	1.91/29	1.56/23	1.00/15

The specimen machining plan and the schematic for specimen ID are shown in Figure 2.2 and Figure 2.3, respectively. For each BFB, four bend bar specimens and seven thin slice specimens were machined. The bend bar specimens were used in the fracture toughness and fatigue crack growth rate studies, whereas the thin slice specimens are planned for subscale tensile and microstructural analyses. Specimens were machined from different fluence regions of each bolt, allowing for studies of the effect of fluence on the microstructural and mechanical properties of BFBs. Three thin slice specimens were machined from the high-stress concentration region, i.e., the transition between the bolt head and shank, of each bolt to allow for further investigation of possible crack initiation sites.

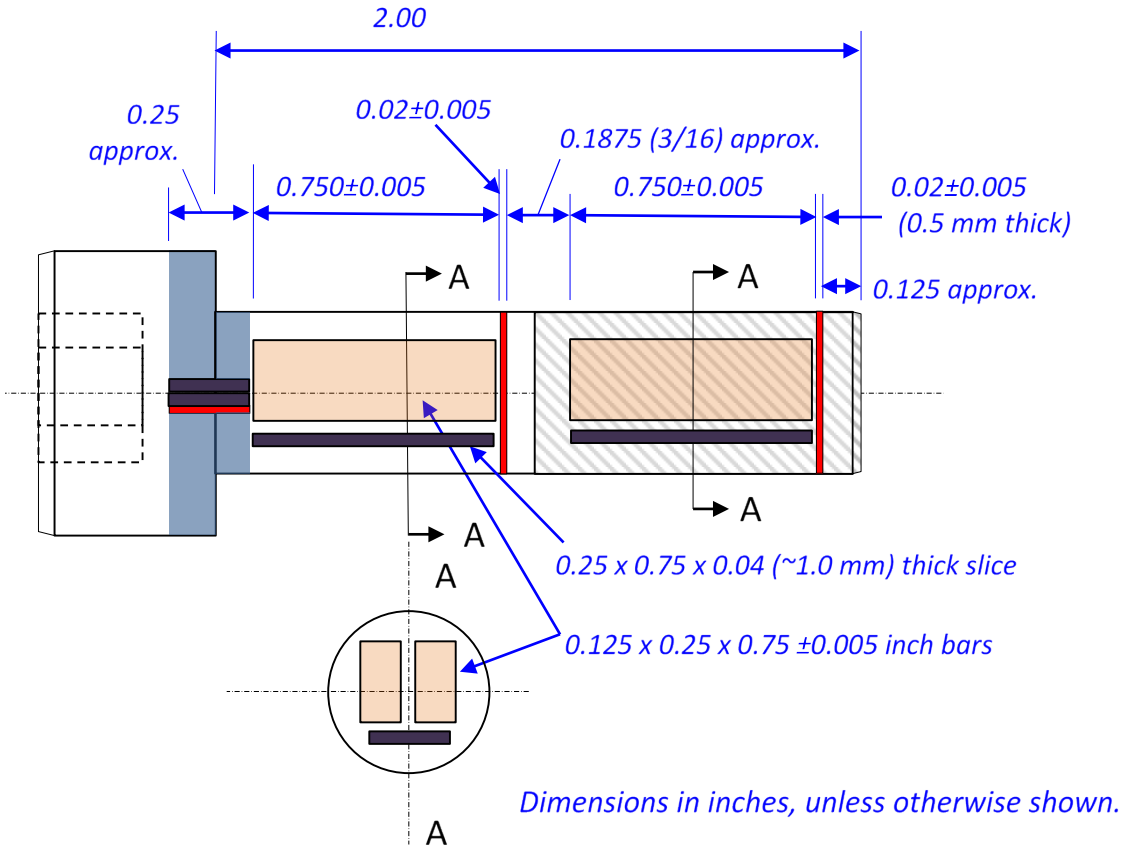

***Figure 2.2**: Machining diagram for the BFBs showing the color-coded sample types (red: 0.5 mm slices, black: 1.0 mm slices, light orange: bend bars, and light blue: remaining collar materials)* [10]

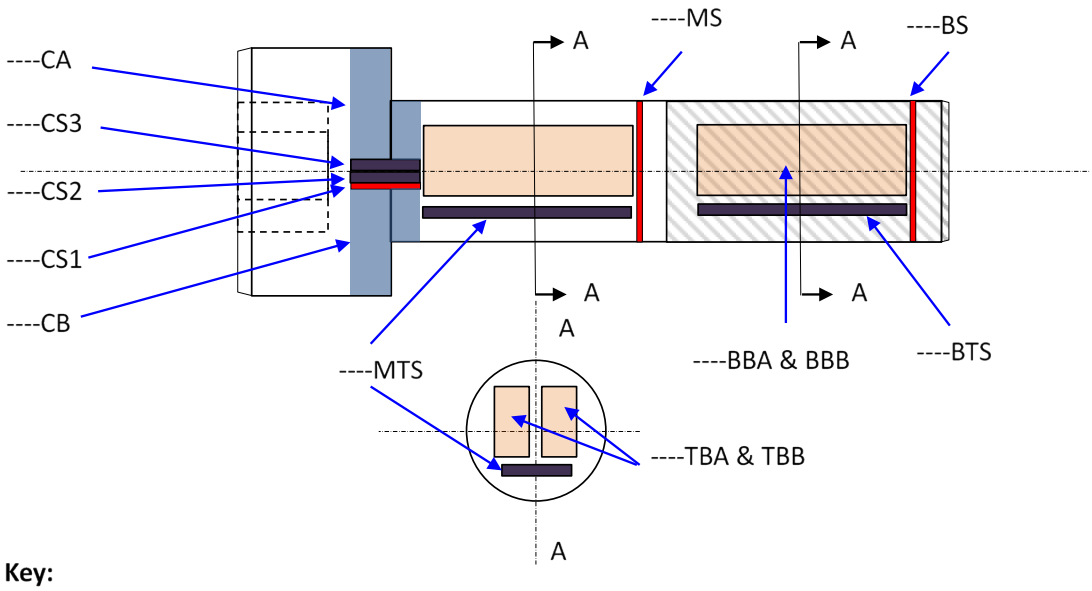

Key:
----: bolt number, **CS**: collar slice, **CA & CB**: remaining collar materials, **MS**: middle slice, **BS**: bottom slice, **MTS**: middle thick slice, **BTS**: bottom thick slice, **TBA & TBB**: top bend bar, **BBA & BBB**: bottom bend bar

***Figure 2.3**: Schematic for sample IDs from machined BFBs* [10]

2.2 Characterization Methods

Detailed APT and scanning electron microscopy (SEM) characterizations were performed on the thin slice specimens. In detail, after mechanically polished to mirror-surface conditions, thin slice specimens from BS, MS, and CS sections were loaded into a Thermo Fisher Versa3D focused ion beam (FIB)/SEM DualBeam™ system, where needle shaped-type speciemns were lifted-out and shaped for APT characterizations (and previously, lamella were lifted out for TEM characterization). The APT sample preparation followed the procedures of depositing a protective layer of Pt/C followed by undercutting at a 30° angle before being lifted out and put on Si multi-post arrays. Tips were sharpened using gradual annular milling using 30 keV Ga ions to a tip diameter of 100-150 nm. Final polishing was performed using 2 keV Ga ions to reduce the amount of implanted Ga, which could change the precipitation density inside the material.

APT was performed on a Cameca LEAP 4000XHR using laser pulse mode with a laser energy of 60 pJ, detection rate of 0.005 atoms/pulse, pulse repetition rate of 200 kHz while maintaining needle specimen temperature at ~40 K. Reconstructions and analyses for APT were performed using Cameca's Integrated Visualization and Analysis Software 3.8.10 (IVAS) using techniques that include radial distribution functions (RDF) analysis, frequency distribution analysis, and isoconcentration surface (isosurface)-based cluster analysis [11–13]. Similar mass/charge range files with only minor adjustments in the widths of selected peaks between reconstructions were used to reduce potential artefacts in compositional analyses among the various samples. The tip profile reconstruction method was used for determining the initial radius of the reconstruction using high resolution SEM images of the final tip. A fixed image compression factor of 1.65 and k-factor of 3.30 was used as no clear pole locations were found within the field ion micrographs. Global background subtraction was used for determining composition. Peak overlaps were considered and adjusted based on relative natural abundance of specific isotopes and preferred evaporation

charge state; in general, these overlaps had a minimal effect for the purposes of this study as the greatest overlap accounted for less than 5% of a particular element (isotope 54 with overlaps for Cr and Fe).

Cluster analysis in APT data is a common unsupervised machine learning problem, and like many other problems in this category, it lacks a clear metric/loss function to define a quality of prediction or a confidence level of the result. In this study, we used the isosurface method for Ni, Si, Mo, and Cu clusters identification [14,15]. It is a simple and widely used technique to identify clusters by constructing a constant concentration surface based on local solute concentration, and the enclosed ions are identified as a cluster. This technique has great flexibilities and needs only one user input as concentration threshold. The concentration threshold is kept constant for all datasets since we are interested in the cluster size evolution, which is directly affected by the threshold choice. However, the selection of parameters may lead to some uncertainties for cluster identification in conditions where precipitation is low (i.e., low temperature thermal aging or irradiation). This is due to some clusters having much lower solute concentration in these conditions. However, we believe the corresponding volume fraction trend is preserved despite the minor uncertainties.

RDF analyses of individual elements in APT data enables understanding of not only the extent with which the elements segregate but also to which other elements they are most strongly attracted to or repulsed by [13,16]. RDF analysis provides an average radial concentration around each atom in the APT reconstruction data for a particular element as a function of radial distance from the center atom. This average radial concentration profile for each element, when divided by the average bulk concentration of that element, provides the bulk normalized concentration plots. A value of 1 for bulk normalized concentration corresponds to a random distribution or no correlation with the designated element. A value above 1 indicates attraction with the "center atom" element. A value less than 1 indicates a repulsive interaction with the designated element.

Since it was revealed that the exposed surface of the bolts was still intact at the region where the bolt head meets the bolt shank, further characterization was performed on this region of the collar slice and this characterization is ongoing. The collar slice or CS section of BFB #4412 was the first bolt to be characterized. It was imaged using a Tescan Mira3 SEM equipped with a Oxford Instruments Symmetry electron backscatter diffraction (EBSD) detector and Oxford Instruments energy dispersive X-ray spectroscopy (EDS) detector. The cross-section near the curved region was investigated for cracks that may hint at in-service IASCC. Detailed SEM imaging and EBSD and EDS maps were taken from this area.

3. RESULTS AND DISCUSSION

3.1 APT Characterization

As reported previously [2,3], TEM and STEM characterization revealed heavily evolved microstructures in all of the sections of both baffle-former bolts during service, with high densities of dislocations, precipitation, and cavity formation. Additionally, radiation-induced grain boundary segregation was found in both bolts in each section of the bolts at high angle grain boundaries only. There was no segregation to low angle grain boundaries. Using TEM/STEM characterization and analysis, it was found that the BS and MS sections of both bolts had bimodal distributions of nanoscale cavities of about 2 nm in diameter and 8 nm in diameter, while the CS section only has the small size cavities. Both bolts showed the same cavity distribution along the length of the bolts with no clear difference between the bolts. The STEM-EDS analysis was mostly qualitative for the relative amount of radiation-induced precipitation of Ni/Si-rich clusters in each section of the bolts and did not provide a clear differentiation between the two bolts. The lack of a clear qualitative or even semi-quantitative difference among the different locations in each bolt and between bolts with respect to precipitation and segregation highlights the need for a more quantitative characterization technique, which APT provides. We report here the quantitative extent of precipitation for

each bolt section for both bolts. Future work in FY24 will emphasize APT work on the grain boundary segregation.

APT characterization complements TEM/STEM characterization quite well, as it is a technique that enables higher spatial and compositional resolution all in three spatial dimensions; though it can struggle to identify cavities or structural features without elemental segregation. Here, APT data were collected from the matrix from each of the three sections in both bolts. Future work coming in FY24 will target the grain boundaries in these sections. First, the atomic and isosurface reconstructions will be shown followed by analytical information to determine trends in elemental segregation. Figure 3.1 depicts atom reconstructions and isosurface reconstructions, respectively, from one reconstruction of each section of both bolts. While it is difficult to semi-quantitative determine the relative degree of precipitation looking directly at the precipitates, it perhaps is more easily captured by looking at the matrix or "background" atoms in each section of both bolts in Figure 3.1(a), particularly for BFB #4412, where it appears that Ni, Si, and Mo are faintest in the BS reconstruction, while Cu is faintest in the CS reconstruction. This partially shows which precipitates form and under what conditions (Ni/Si and Mo preferentially in BS, and Cu in CS). The isosurface reconstructions in Figure 3.1(b) show similar trends in BFB #4412 but less so in BFB #4416; there appears to be a larger fraction of Ni/Si precipitation in the BS and MS reconstructions than in the CS section and more Cu precipitation in the CS section. There is a qualitative difference between the two bolts based on the visualizations in Figure 3.1: the Ni/Si precipitation does not appear particularly different in each section of the bolt in BFB #4416, unlike in BFB #4412. To be discussed later, this difference could be an indication of different irradiation temperature profiles between the two bolts. As shown previously [3], the red Mo and orange Cu isosurfaces are slightly separate from the Ni/Si isosurfaces and in many cases attached to the Ni/Si isosurfaces providing evidence of complex precipitation structures.

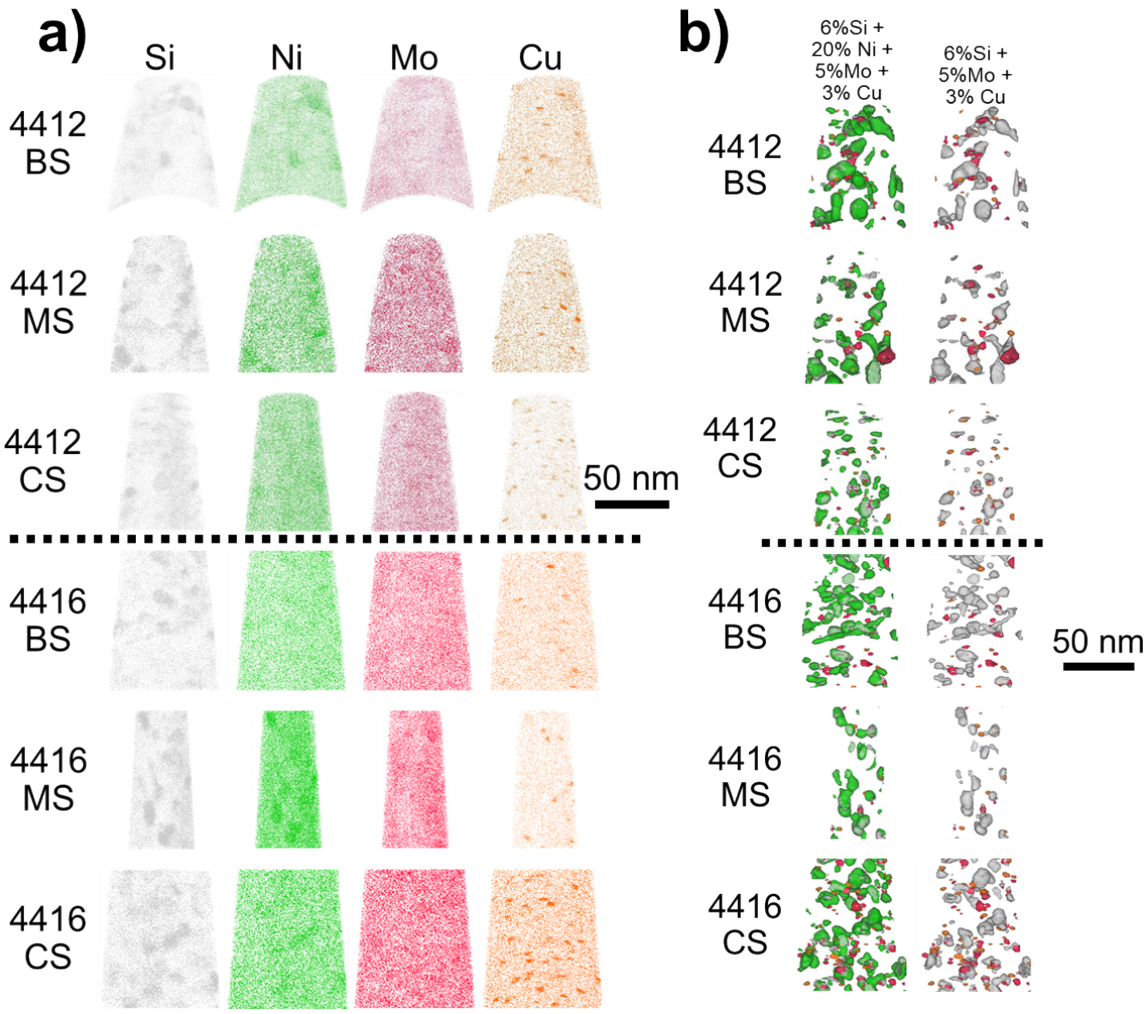

Figure 3.1*: a) Atom reconstructions of Si, Ni, Mo, and Cu atoms from a select reconstruction of each section of both bolts. The reconstructions here are 30 nm in thickness. b) Isoconcentration surface (isosurface) reconstructions of same regions through the full thickness of the reconstruction. Green isosurfaces are of 20at% Ni, gray isosurfaces are of 6at% Si, red isosurfaces are of 5at% Mo, and orange isosurfaces are of 3at% Cu.*

APT characterization allows for a high degree of quantification beyond standard visualization. Figure 3.2 shows the volume fraction and average spherical-equivalent radius of Ni-20at%, Si-6at%, Mo-5at%, and Cu-3at% isosurfaces averaged over the reconstructions from each section of both bolts. In both bolts, the volume fraction and radius of Ni and Si isosurfaces is highest in the thread or BS section and lowest in the head or CS section. Comparing the two bolts, the trends of BS > MS > CS for the volume fraction holds, but overall the degree of Ni and Si clustering is greater in the high dose bolt #4412, especially in the bolt thread or BS section. This suggests that Ni and Si clustering has not hit a steady-state and that these precipitates can continue to form and particularly grow with increasing dose at the highest irradiation temperature found in the bolt thread end, assuming temperature profile matches Ref. [5]. The Mo isosurfaces appear to have no clear trends as the volume fraction and radius is highest in the mid-shank for the high dose BFB #4412 but lowest in the mid-shank for the low dose BFB #4416. These differences in trends for Mo may indicate the irradiation temperature profile is slightly different between the two bolts and not always consistent with Ref. [5]. Generally though, it seems the variation for Mo isosurfaces is minimal. On the other hand, the volume fraction of Cu isosurfaces is highest in the CS section compared to

the BS and MS sections for both bolts. Comparing the two bolts, shows that Cu precipitation has not changed with increasing dose, suggesting it has hit a steady-state by the dose in the lower dose bolt.

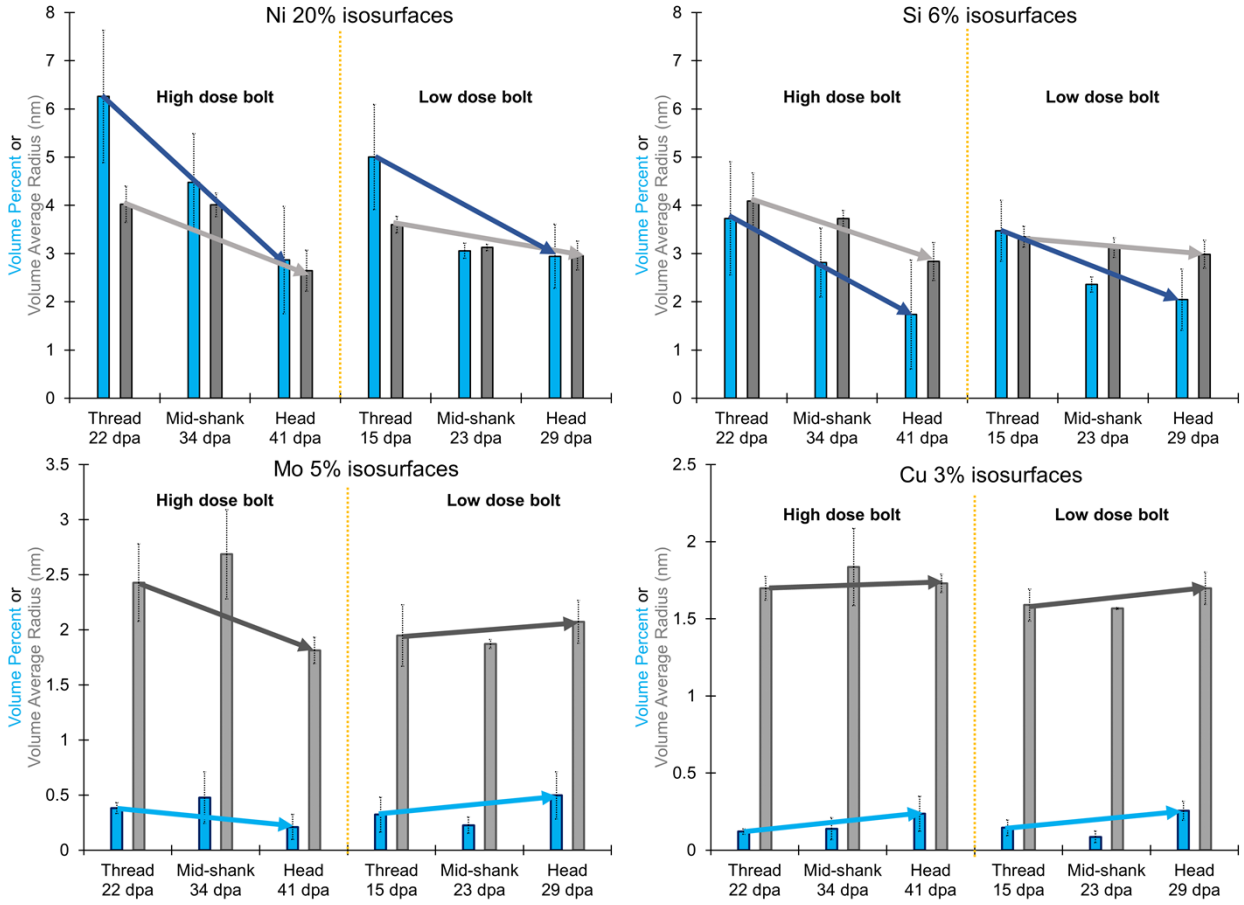

***Figure 3.2**: Volume percent (in blue) and volumetric average spherical equivalent radius (in grayf 20at% Ni, 6at% Si, 5at% Mo, and 3at% Cu isosurfaces averaged over four reconstructions for each section of the BFB #4412 and 2-5 reconstructions for BFB #4416. Error bars represent one standard deviation.*

As mentioned in section 2.2, using isosurfaces to determine clustering is imprecise and depends on an arbitrary at% input and on the quality of the reconstruction as clustering is highly localized. To remove some of the arbitrariness and still identify and determine trends, frequency distribution analysis (Figure 3.3) and RDF analysis (Figure 3.4, Figure 3.5, Figure 3.6, and Figure 3.7) were performed. Frequency distribution analysis spatially groups together atoms into bins of 200 atoms – in this case, calculates the concentration of each element in those bins, and then determines the frequency of a given concentration over the entire reconstruction. After phase separation as a result of irradiation, the shape of the peaks change relative to binomial distribution, as shown in Fiugre 3.3(a), with some bins becoming purer in Fe, while others become more concentrated in Ni, Si, or Cu. Furthermore, Pearson correlation coefficient analysis uses the frequency distributions to identify the degree of phase separation. The Pearson correlation coefficient (μ) is based on the chi square (χ^2) test with datasets that vary in size, which is useful here as the APT reconstructions are not of the same size for the different reconstructions [12]. Figure 3.3(b) shows the Pearson correlation coefficient for Fe, Cr, Ni, Si, Mn, Mo, and Cu. The value of μ is between 0 and 1, with 0 corresponding to fully homogeneous and 1 to a high degree of phase separation. For the higher dose BFB #4412, it is clear that Fe, Cr, Ni, and Si have more elemental segregation in the BS and MS sections of the bolt than in the CS section of the bolt and that the BS and MS sections are nearly the same. Elemental separation of Mo follows the same trend as that of Mo isosurfaces from Figure 3.2. On the other hand, Cu

has more elemental separation in the CS section of the bolt than the BS and MS sections. In general, the trends observed from the isosurface analysis are back up by the frequency distribution analysis and the Pearson correlation analysis for each of the two bolts. However, the degree of Ni and Si elemental separation does not seem nearly as drastic as that seen in the isosurface analysis.

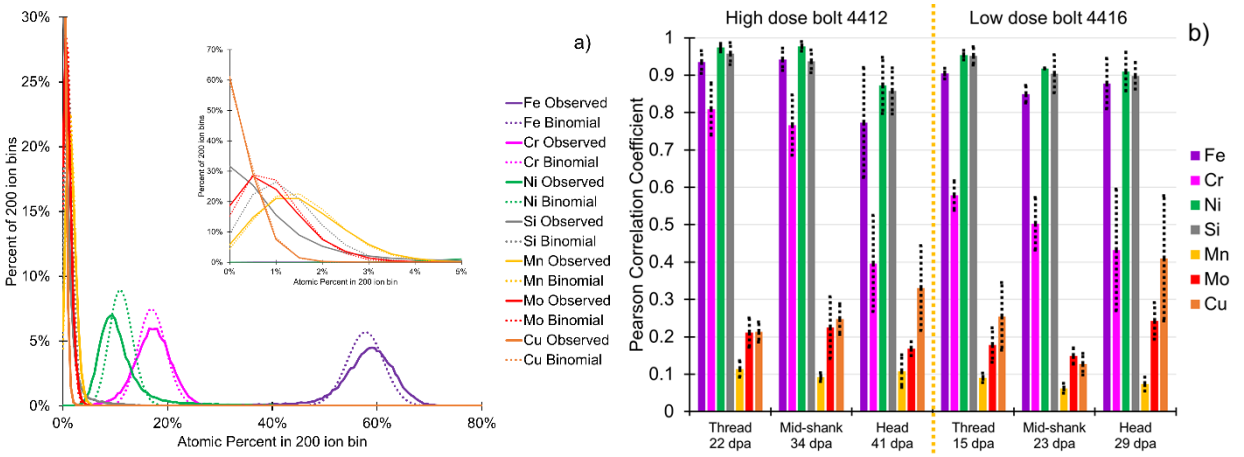

Figure 3.3*: a) Example frequency distribution of 200-ion bins and binomial distribution of elements based on reconstruction concentration from BS tip 3 of BFB #4412. b) Pearson correlation coefficients of Fe, Cr, Ni, Si, Mn, Mo, and Cu atoms averaged over four reconstructions for each section of the BFB #4412 and 2-5 reconstructions for each section of the BFB #4416, based on doing frequency distribution analysis. Error bars represent one standard deviation.*

Taking the frequency distribution analysis further, RDF analysis now only shows the degree of elemental separation but also to which elements they segregate to or from. RDF analysis of all reconstructions from each bolt present the bulk normalized concentration of certain elements as a function of distance from Ni, Si, Cr, Mo, and Cu atoms, respecitvely, in Figure 3.4, Figure 3.5, Figure 3.6, Figure 3.7 and Figure 3.8. Values greater than 1 indicate attraction and values less than 1 indicate repulsion. Looking at the concentration near Ni atoms in Figure 3.4, Ni and Si segregation to Ni atoms is higher in the BS and MS sections, which likely have a higher irradiation temperature, than the CS section despite it having a higher dose. Separation of Cr and Mo from Ni atoms follows the same trend of BS > MS > CS. Mn has slight segregation or no segregation to Ni in the CS sections but does segregate away from Ni in the MS and BS sections. Cu segregates to Ni atoms, but it has no particular trend between the different secitons of the bolts toward Ni atoms as the variation between tips and even between bolts effectively makes them all the same. The trends among the three sections are the same for both bolts but is generally more muted in the low dose bolt #4416. Interestingly though, the level of segregation of each element to or from Ni in the CS sections of both bolts is effectively the same. This suggests that the bolt head, and the temperature there, are nearly at a steady-state for elemental segregation, but the bolt mid-shank and thread are not in a steady-state.

Segregation to and/or from Si as shown in Figure 3.5 largely follows the same trends as that of Ni in Figure 3.4. The key differences though are that 1) Ni and Si segregation to Si and Cr segregation from Si are at much stronger values than that of Ni and Si to Ni and Cr from Ni, and 2) that Mo segregates to Si atoms in the CS section of both bolts and away from Si in the MS and BS sections, unlike with Ni, where Mo is always segregating away from Ni. This suggests that Si and not Ni may be the primary driver of precipitation. Since the higher concentration Ni remains within the matrix to a higher degree, it is not able to facilitate precipitation as much as Si.

In Figure 3.6, segregation away from Cr by Ni and Si and to Cr by Cr, and Mn follows similar trend with greatest segregation in BS section and least in CS section. However, the degree of segregation is essentially

the same between the two bolts. Compared to segregation to and from Mo in Figure 3.7, the higher concentration Cr shows less segregation just like Ni relative to Si. Segregation to and from Mo behaves similarly to segregation to and from Si. The BS section has the greatest segregation and the CS section has the least segregation of Ni and Si away (or no segregation) from Mo and Mn, Cr, and Mo towards Mo. Additionally, just like Ni and Si, the high dose bolt #4412 has more segregation in the BS and MS sections than in the same sections in the lower dose bolt #4416. On the other hand, Cu essentially has no preference to segregate to or away from Mo atoms, and this does not change between the two bolts. The segregation to and from Mo and Cr confirms the precipitation of the Cr-Mo-rich phase that was attached to the Ni/Si-rich precipitatse in the 2D concentration contour plots and STEM-EDS maps presented previously [3]**Error! Reference source not found.**.

Lastly, in Figure 3.8, segregation of every other element to or from Cu is modest and follows no trends, but Cu segregation to itself is high and follows the inverse trend of Ni/Si/Mo, where the CS section has by far the greatest degree of elemental segregation for Cu and the BS section has the least degree of segregation of Cu to Cu. The Cu clustering is similar but slightly higher in the high dose bolt #4412 than in the lower dose bolt #4416. These results confirms the insights gained from the isosurface analysis.

The conclusions and hypotheses stated in the previous APT analysis on BFB #4412 alone [3] have been proven to be mostly true. The Cu clustering may have a higher dependence on radiation dose than on temperature as Cu is likely to phase separate at any elevated temperature due to its low miscibility in Fe and Cr; however, as newly found based on BFB #4416, the saturation dose for Cu clustering is lower than what is seen in BFB #4416. As Cu clustering is highest in the CS sections and Ni/Si clustering remains unchanged between the bolts in the CS sections, the lower irradiation temperature has likely reached a steady-state or the kinetics are very slow at this temperature. Reiterating from the previous report, Cu precipitation has a higher dependency on vacancy concentration than on vacancy or atomic mobility, whereas Ni/Si precipitation may have the opposite dependency. Ballistic mixing during radiation generally favors dissolution of Ni and Si into FCC Fe, while the thermal spikes during irradiation are enough to cause Cu precipitation, independent of temperature, but as the temperature rises, ballistic mixing of Ni and Si is overcome by back diffusion due to a bias for phase separation [17]. A large change in temperature is not necessarily needed to see this drastic difference in precipitation as a change in thermal aging of duplex stainless steels from ~290 °C to 330 °C goes from no precipitation to significant level after 30,000 hours of aging [15,16]. As hypothesized for the lower dose BFB #4416, it was expected and turned out to be correct that the volume fraction would be similar or slightly lower for the Cu clusters, while the Ni/Si-rich clusters will likely have a smaller radius but similar number density. Interestingly, these precipitation trends of Ni/Si and Cu in austenitic stainless steels are consistent with Cu-rich precipitation and Mn-Ni-Si-rich precipitation in reactor pressure vessel steels [18,19].

Combining the APT analysis of both bolts with the cavity analysis from TEM [2,3] reveals that there are gradients in temperature, strain, and fast/thermal neturon energy from one end of the bolt to other. These effects appear to overcome the 2X difference in radiation dose from one end of the bolt to the other. Vacancies are much more mobile due to thermal and strain gradients where they can gather into vacancy clusters and grow into large cavities and enhance the growth of Ni/Si-rich precipitates. This is consistent with analysis of a baffle-former bolt retrieved from the Tihange 1 reactor [9] and with variation in void swelling in thick components [20]. Comparing with mechanical behavior analysis [2], the same gradient in Ni/Si precipitation in BFB #4412 is found in the Vicker's hardness with the thread section having the highest hardness. For the lower dose bolt #4416, the relatively suppressed Ni/Si precipitation relative to the higher dose bolt corresponds with no significant difference in hardness along the length of the bolt. And the extent of Ni/Si precipitation (and segregation of Ni and Si) in the lower dose bolt being similar to the CS section of the higher dose bolt corresponds with the hardness of all sections of the lower dose bolt being the same as the hardness of the CS section in the higher dose bolt [2]. The drop in fracture toughness in the MS and BS sections in both bolts [4] also follows with the trends in Ni/Si precipitation found here.

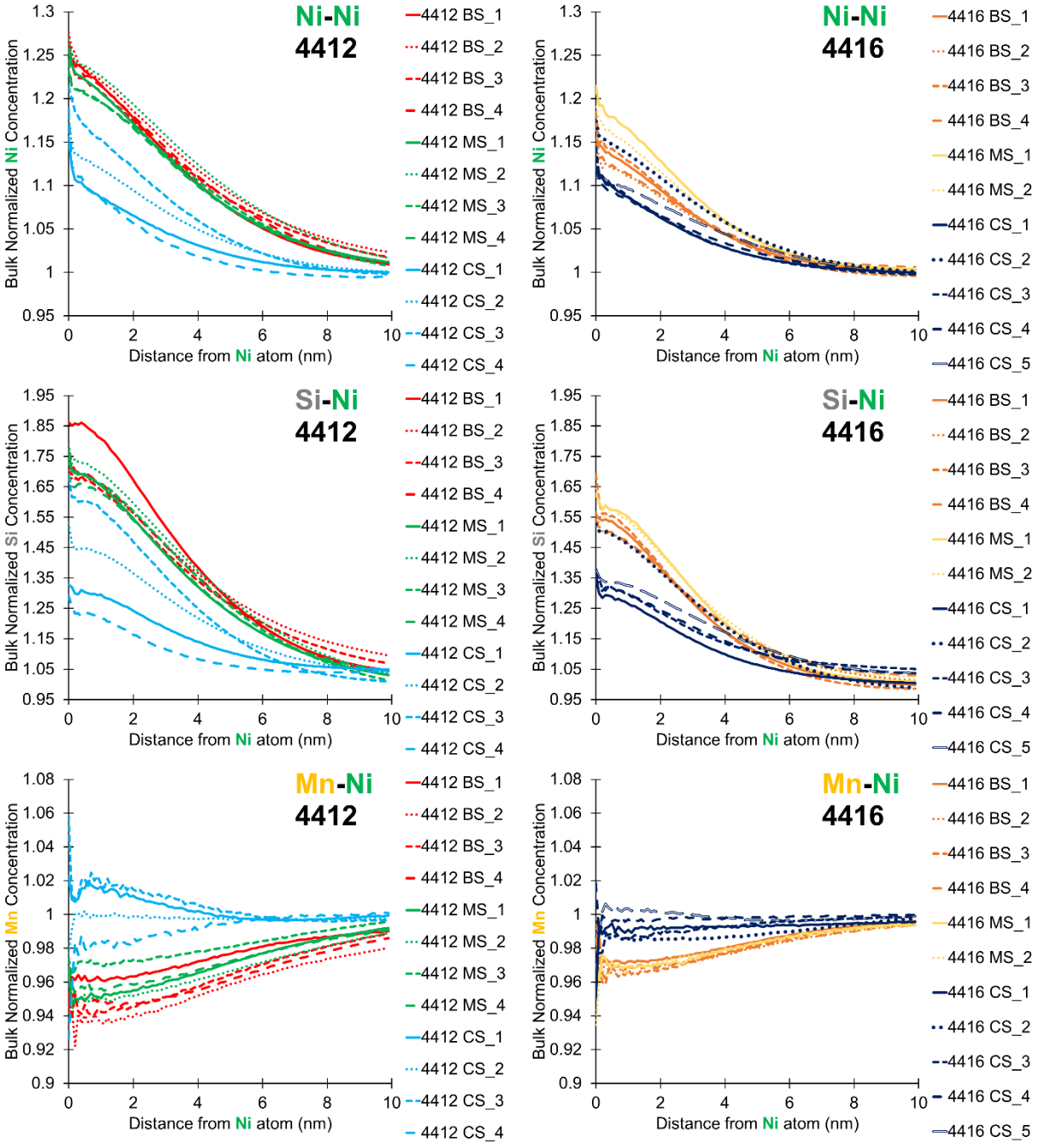
Ni-Ni
4412
Bulk Normalized Ni Concentration
Distance from Ni atom (nm)
4412 BS_1
4412 BS_2
4412 BS_3
4412 BS_4
4412 MS_1
4412 MS_2
4412 MS_3
4412 MS_4
4412 CS_1
4412 CS_2
4412 CS_3
4412 CS_4
Ni-Ni
4416
Bulk Normalized Ni Concentration
Distance from Ni atom (nm)
4416 BS_1
4416 BS_2
4416 BS_3
4416 BS_4
4416 MS_1
4416 MS_2
4416 CS_1
4416 CS_2
4416 CS_3
4416 CS_4
4416 CS_5
Si-Ni
4412
Bulk Normalized Si Concentration
Distance from Ni atom (nm)
4412 BS_1
4412 BS_2
4412 BS_3
4412 BS_4
4412 MS_1
4412 MS_2
4412 MS_3
4412 MS_4
4412 CS_1
4412 CS_2
4412 CS_3
4412 CS_4
Si-Ni
4416
Bulk Normalized Si Concentration
Distance from Ni atom (nm)
4416 BS_1
4416 BS_2
4416 BS_3
4416 BS_4
4416 MS_1
4416 MS_2
4416 CS_1
4416 CS_2
4416 CS_3
4416 CS_4
4416 CS_5
Mn-Ni
4412
Bulk Normalized Mn Concentration
Distance from Ni atom (nm)
4412 BS_1
4412 BS_2
4412 BS_3
4412 BS_4
4412 MS_1
4412 MS_2
4412 MS_3
4412 MS_4
4412 CS_1
4412 CS_2
4412 CS_3
4412 CS_4
Mn-Ni
4416
Bulk Normalized Mn Concentration
Distance from Ni atom (nm)
4416 BS_1
4416 BS_2
4416 BS_3
4416 BS_4
4416 MS_1
4416 MS_2
4416 CS_1
4416 CS_2
4416 CS_3
4416 CS_4
4416 CS_5

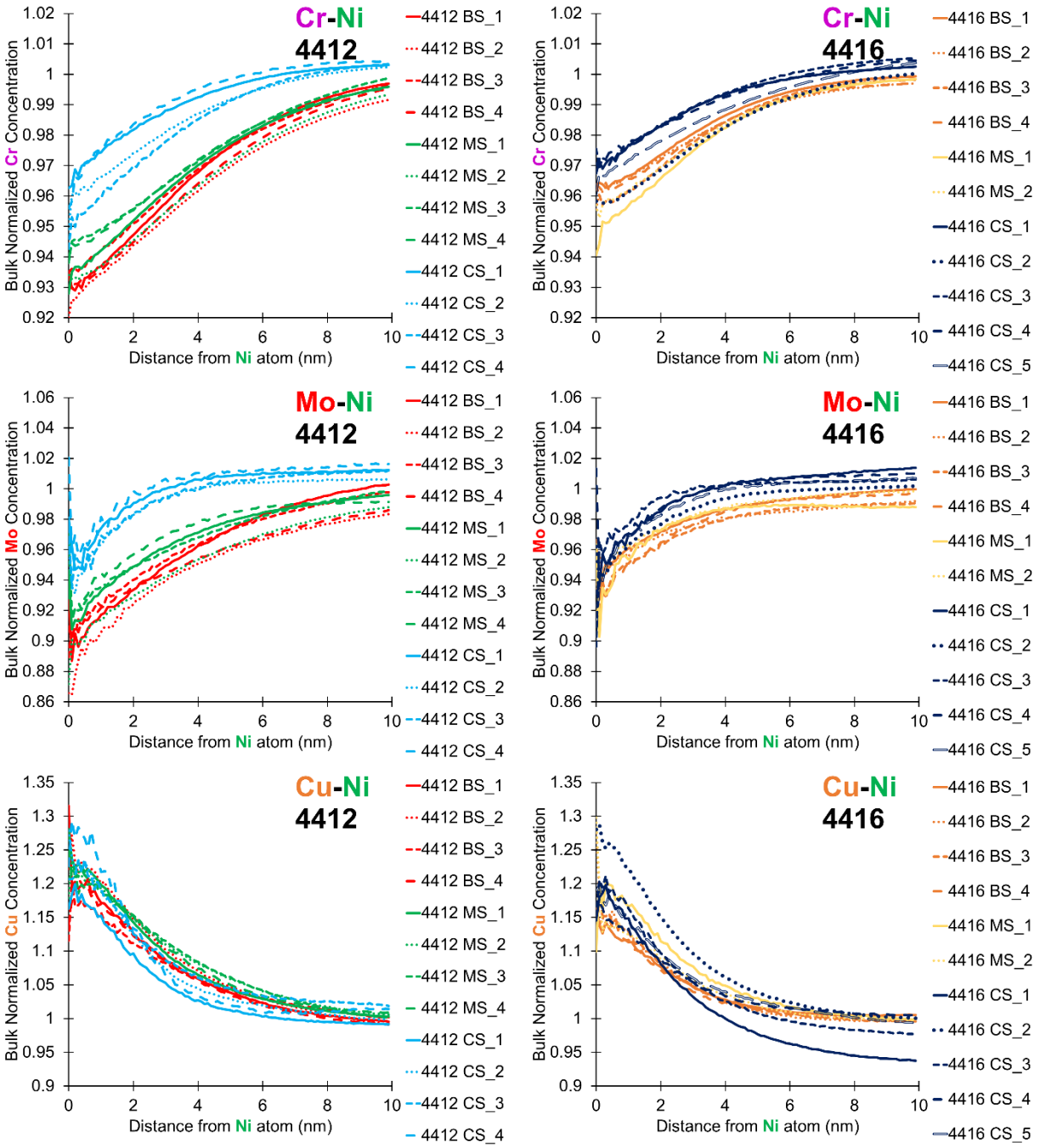

***Figure 3.4**: Bulk normalized Ni, Si, Mn, Cr, Mo, and Cu concentrations as a function of distance from a generic Ni atom for each of reconstructions for each section of BFB #4412 on the left and BFB #4416 on the right (marked as _1, _2, _3, _4, and _5, respectively), based on doing RDF analysis.*

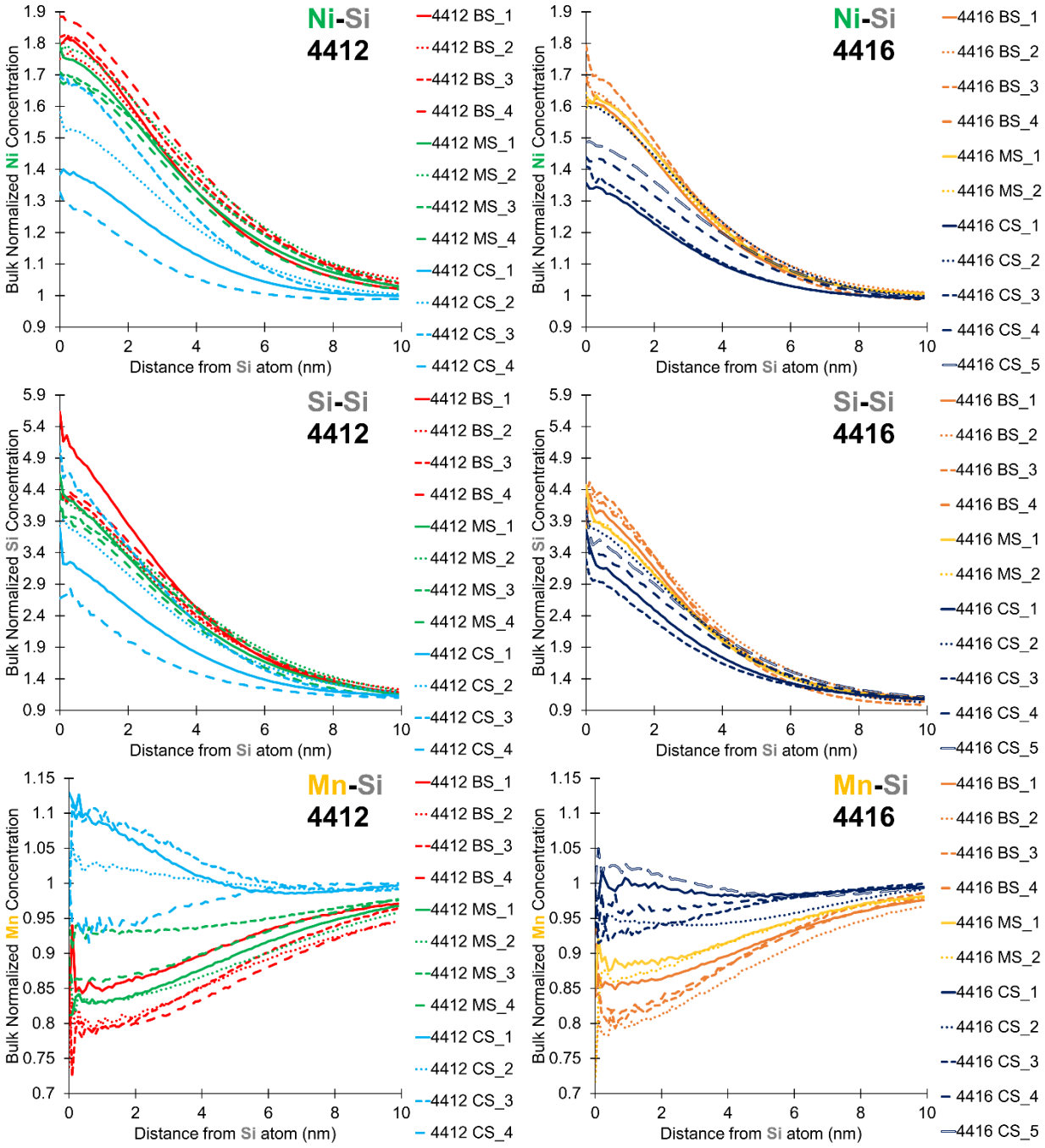
Ni-Si
4412
Bulk Normalized Ni Concentration
Distance from Si atom (nm)
4412 BS_1
4412 BS_2
4412 BS_3
4412 BS_4
4412 MS_1
4412 MS_2
4412 MS_3
4412 MS_4
4412 CS_1
4412 CS_2
4412 CS_3
4412 CS_4
Ni-Si
4416
Bulk Normalized Ni Concentration
Distance from Si atom (nm)
4416 BS_1
4416 BS_2
4416 BS_3
4416 BS_4
4416 MS_1
4416 MS_2
4416 CS_1
4416 CS_2
4416 CS_3
4416 CS_4
4416 CS_5
Si-Si
4412
Bulk Normalized Si Concentration
Distance from Si atom (nm)
4412 BS_1
4412 BS_2
4412 BS_3
4412 BS_4
4412 MS_1
4412 MS_2
4412 MS_3
4412 MS_4
4412 CS_1
4412 CS_2
4412 CS_3
4412 CS_4
Si-Si
4416
Bulk Normalized Si Concentration
Distance from Si atom (nm)
4416 BS_1
4416 BS_2
4416 BS_3
4416 BS_4
4416 MS_1
4416 MS_2
4416 CS_1
4416 CS_2
4416 CS_3
4416 CS_4
4416 CS_5
Mn-Si
4412
Bulk Normalized Mn Concentration
Distance from Si atom (nm)
4412 BS_1
4412 BS_2
4412 BS_3
4412 BS_4
4412 MS_1
4412 MS_2
4412 MS_3
4412 MS_4
4412 CS_1
4412 CS_2
4412 CS_3
4412 CS_4
Mn-Si
4416
Bulk Normalized Mn Concentration
Distance from Si atom (nm)
4416 BS_1
4416 BS_2
4416 BS_3
4416 BS_4
4416 MS_1
4416 MS_2
4416 CS_1
4416 CS_2
4416 CS_3
4416 CS_4
4416 CS_5

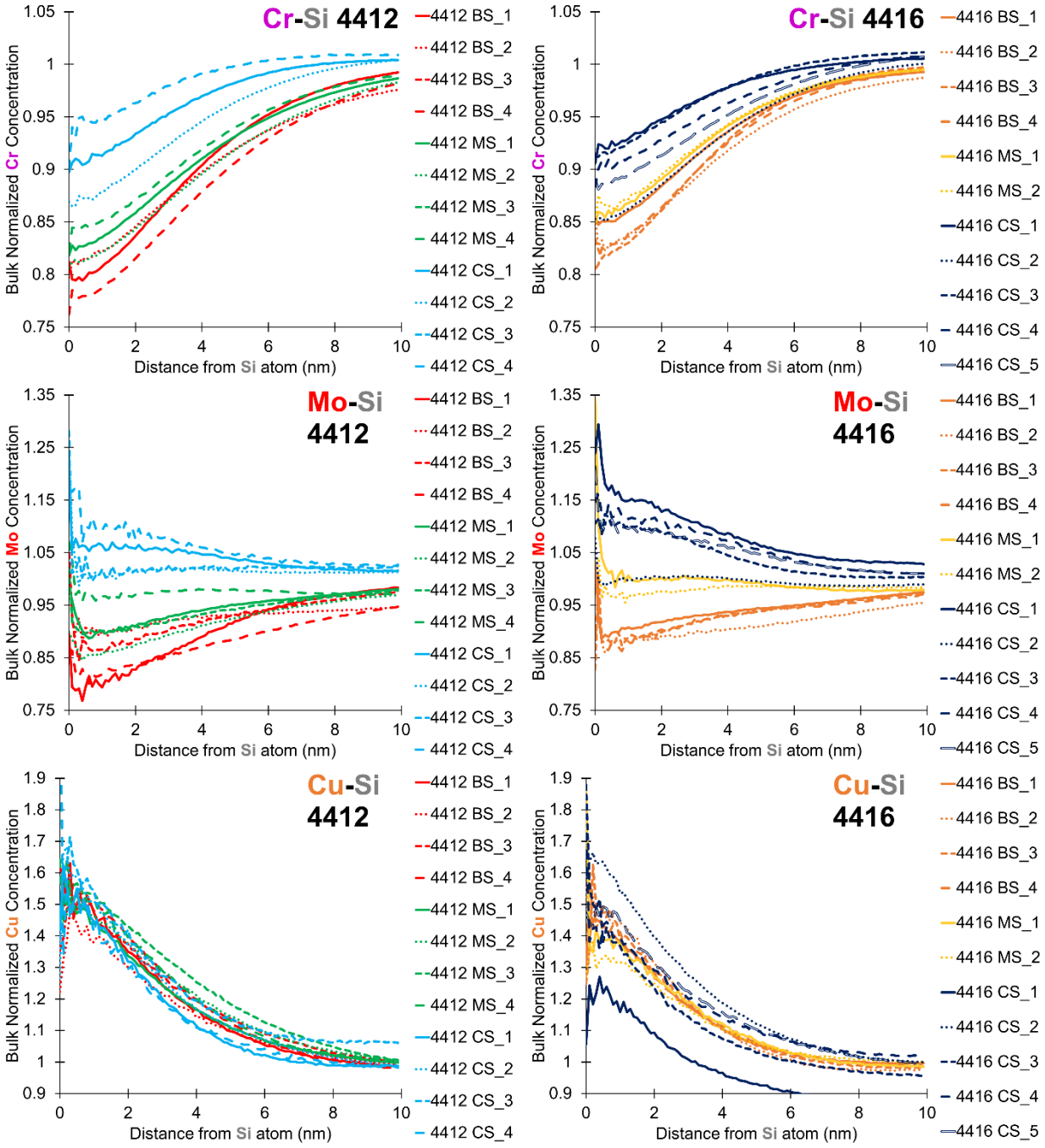

***Figure 3.5**: Bulk normalized Ni, Si, Mn, Cr, Mo, and Cu concentrations as a function of distance from a generic Si atom for each of reconstructions for each section of BFB #4412 on the left and BFB #4416 on the right (marked as _1, _2, _3, _4, and _5, respectively), based on doing RDF analysis.*

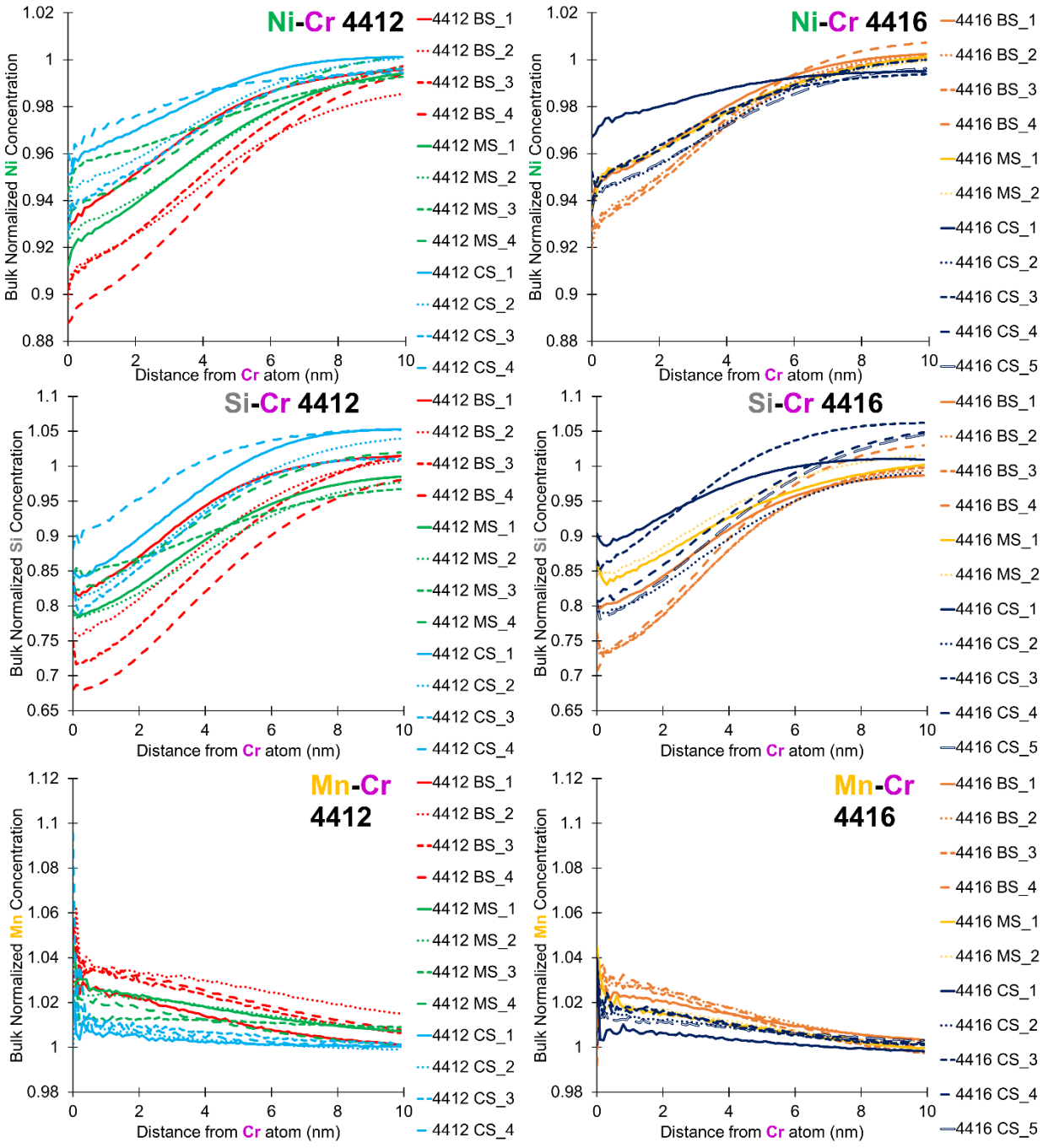
Ni-Cr 4412
Bulk Normalized Ni Concentration
Distance from Cr atom (nm)
4412 BS_1
4412 BS_2
4412 BS_3
4412 BS_4
4412 MS_1
4412 MS_2
4412 MS_3
4412 MS_4
4412 CS_1
4412 CS_2
4412 CS_3
4412 CS_4
Ni-Cr 4416
Bulk Normalized Ni Concentration
Distance from Cr atom (nm)
4416 BS_1
4416 BS_2
4416 BS_3
4416 BS_4
4416 MS_1
4416 MS_2
4416 CS_1
4416 CS_2
4416 CS_3
4416 CS_4
4416 CS_5
Si-Cr 4412
Bulk Normalized Si Concentration
Distance from Cr atom (nm)
4412 BS_1
4412 BS_2
4412 BS_3
4412 BS_4
4412 MS_1
4412 MS_2
4412 MS_3
4412 MS_4
4412 CS_1
4412 CS_2
4412 CS_3
4412 CS_4
Si-Cr 4416
Bulk Normalized Si Concentration
Distance from Cr atom (nm)
4416 BS_1
4416 BS_2
4416 BS_3
4416 BS_4
4416 MS_1
4416 MS_2
4416 CS_1
4416 CS_2
4416 CS_3
4416 CS_4
4416 CS_5
Mn-Cr 4412
Bulk Normalized Mn Concentration
Distance from Cr atom (nm)
4412 BS_1
4412 BS_2
4412 BS_3
4412 BS_4
4412 MS_1
4412 MS_2
4412 MS_3
4412 MS_4
4412 CS_1
4412 CS_2
4412 CS_3
4412 CS_4
Mn-Cr 4416
Bulk Normalized Mn Concentration
Distance from Cr atom (nm)
4416 BS_1
4416 BS_2
4416 BS_3
4416 BS_4
4416 MS_1
4416 MS_2
4416 CS_1
4416 CS_2
4416 CS_3
4416 CS_4
4416 CS_5

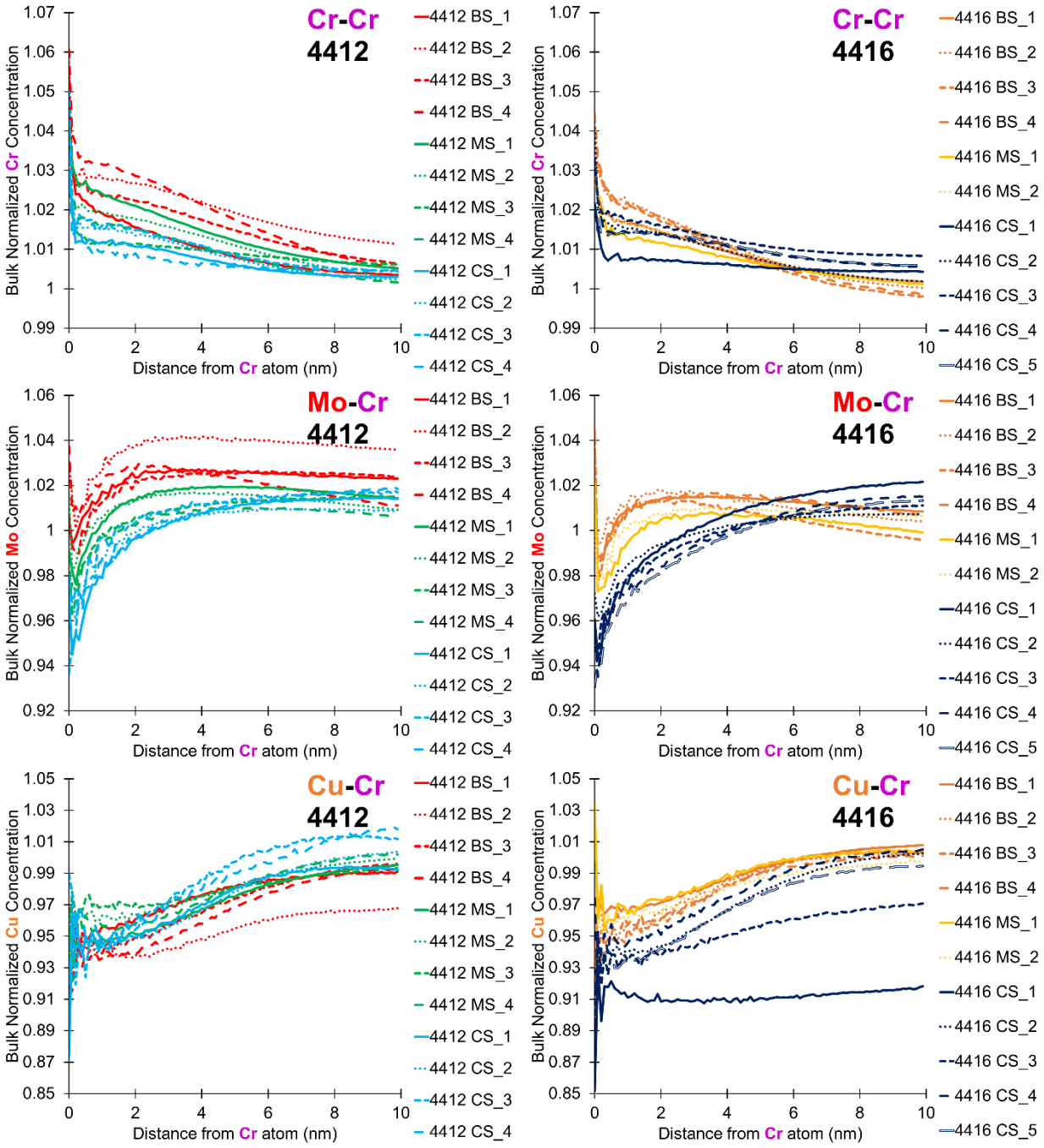

***Figure 3.6**: Bulk normalized Ni, Si, Mn, Cr, Mo, and Cu concentrations as a function of distance from a generic Cr atom for each of reconstructions for each section of BFB #4412 on the left and BFB #4416 on the right (marked as _1, _2, _3, _4, and _5, respectively), based on doing RDF analysis.*

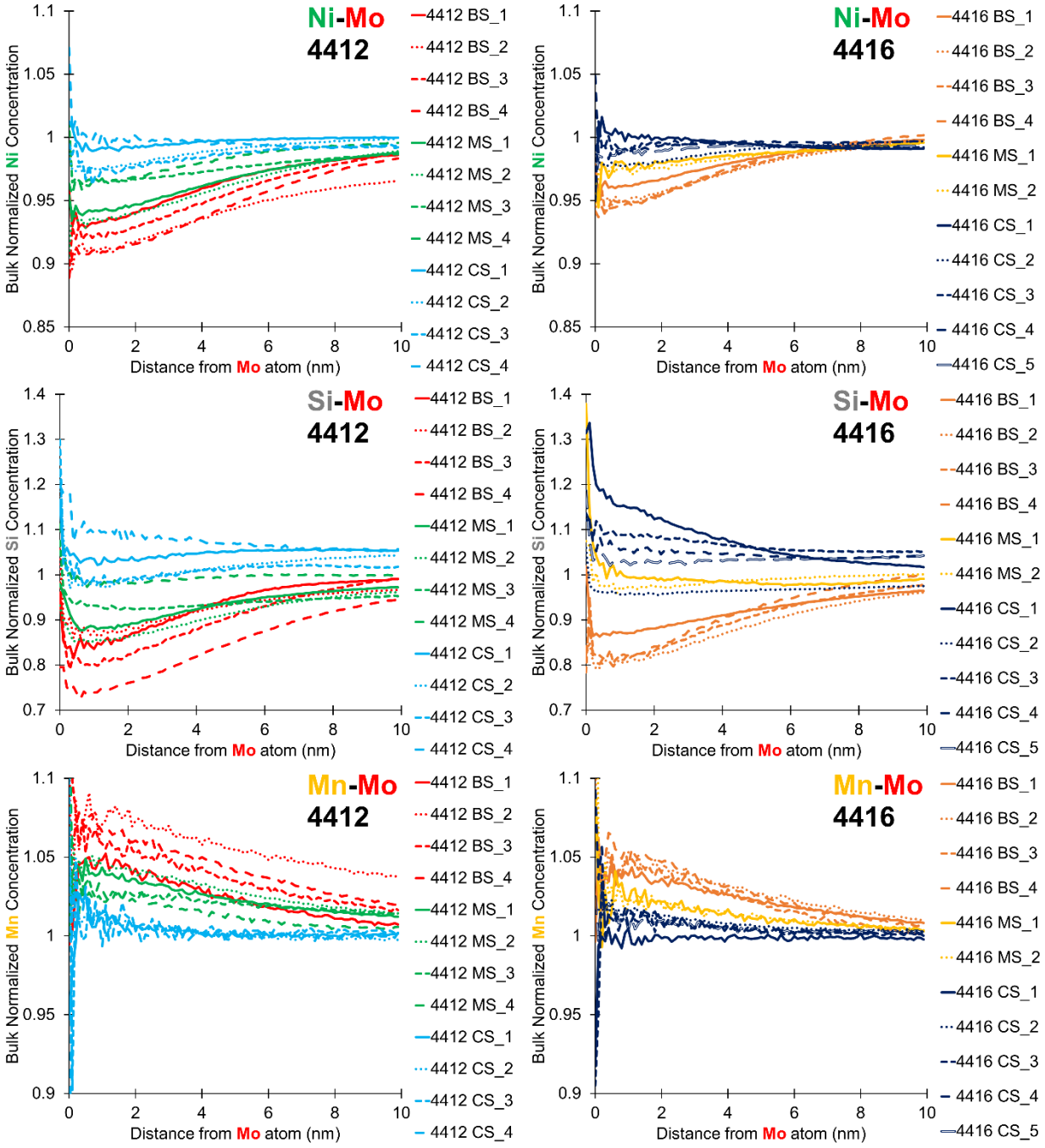
Ni-Mo
4412
Bulk Normalized Ni Concentration
Distance from Mo atom (nm)
4412 BS_1
4412 BS_2
4412 BS_3
4412 BS_4
4412 MS_1
4412 MS_2
4412 MS_3
4412 MS_4
4412 CS_1
4412 CS_2
4412 CS_3
4412 CS_4
Ni-Mo
4416
Bulk Normalized Ni Concentration
Distance from Mo atom (nm)
4416 BS_1
4416 BS_2
4416 BS_3
4416 BS_4
4416 MS_1
4416 MS_2
4416 CS_1
4416 CS_2
4416 CS_3
4416 CS_4
4416 CS_5
Si-Mo
4412
Bulk Normalized Si Concentration
Distance from Mo atom (nm)
4412 BS_1
4412 BS_2
4412 BS_3
4412 BS_4
4412 MS_1
4412 MS_2
4412 MS_3
4412 MS_4
4412 CS_1
4412 CS_2
4412 CS_3
4412 CS_4
Si-Mo
4416
Bulk Normalized Si Concentration
Distance from Mo atom (nm)
4416 BS_1
4416 BS_2
4416 BS_3
4416 BS_4
4416 MS_1
4416 MS_2
4416 CS_1
4416 CS_2
4416 CS_3
4416 CS_4
4416 CS_5
Mn-Mo
4412
Bulk Normalized Mn Concentration
Distance from Mo atom (nm)
4412 BS_1
4412 BS_2
4412 BS_3
4412 BS_4
4412 MS_1
4412 MS_2
4412 MS_3
4412 MS_4
4412 CS_1
4412 CS_2
4412 CS_3
4412 CS_4
Mn-Mo
4416
Bulk Normalized Mn Concentration
Distance from Mo atom (nm)
4416 BS_1
4416 BS_2
4416 BS_3
4416 BS_4
4416 MS_1
4416 MS_2
4416 CS_1
4416 CS_2
4416 CS_3
4416 CS_4
4416 CS_5

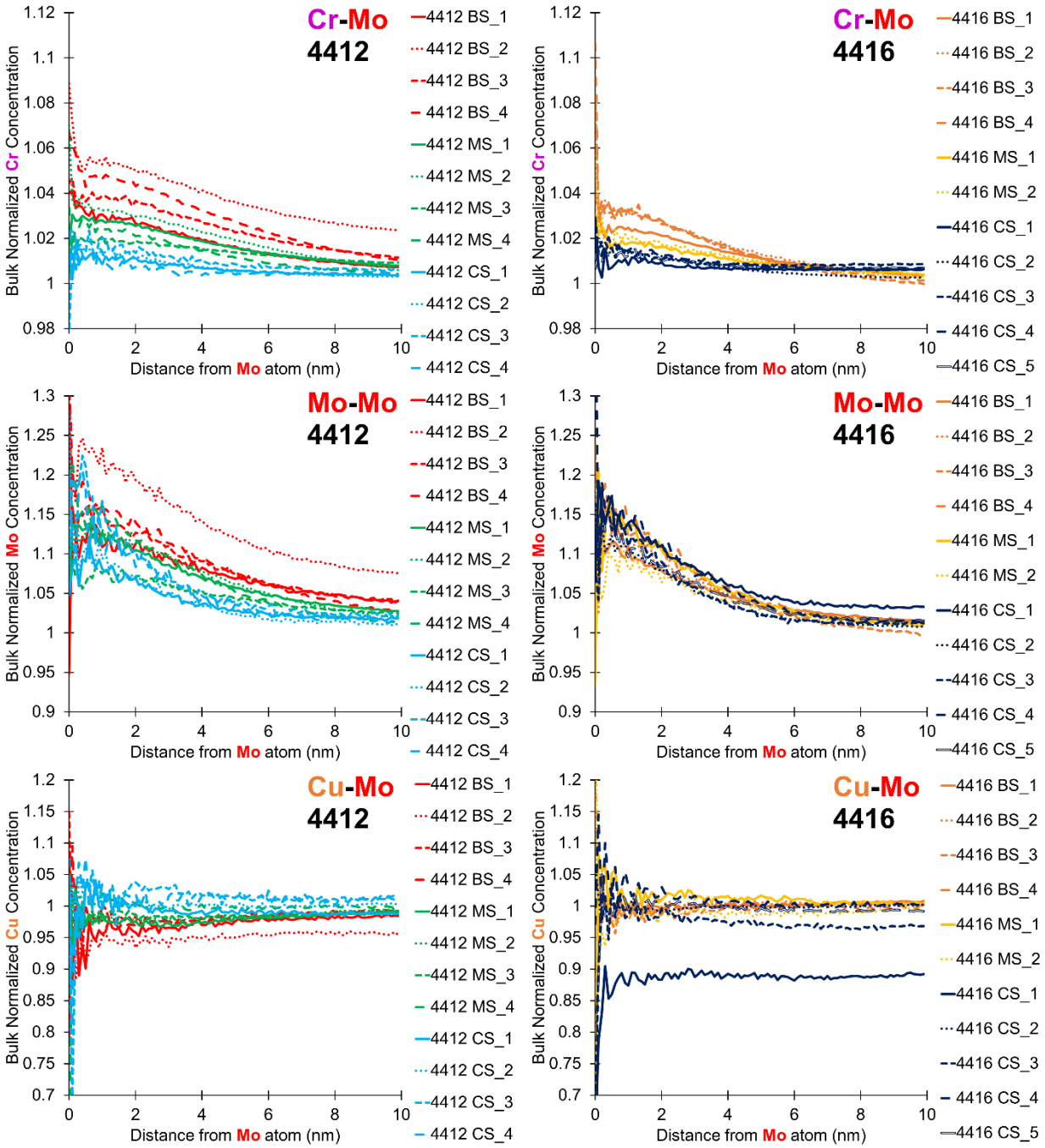

***Figure 3.7**: Bulk normalized Ni, Si, Mn, Cr, Mo, and Cu concentrations as a function of distance from a generic Mo atom for each of reconstructions for each section of BFB #4412 on the left and BFB #4416 on the right (marked as _1, _2, _3, _4, and _5, respectively), based on doing RDF analysis.*

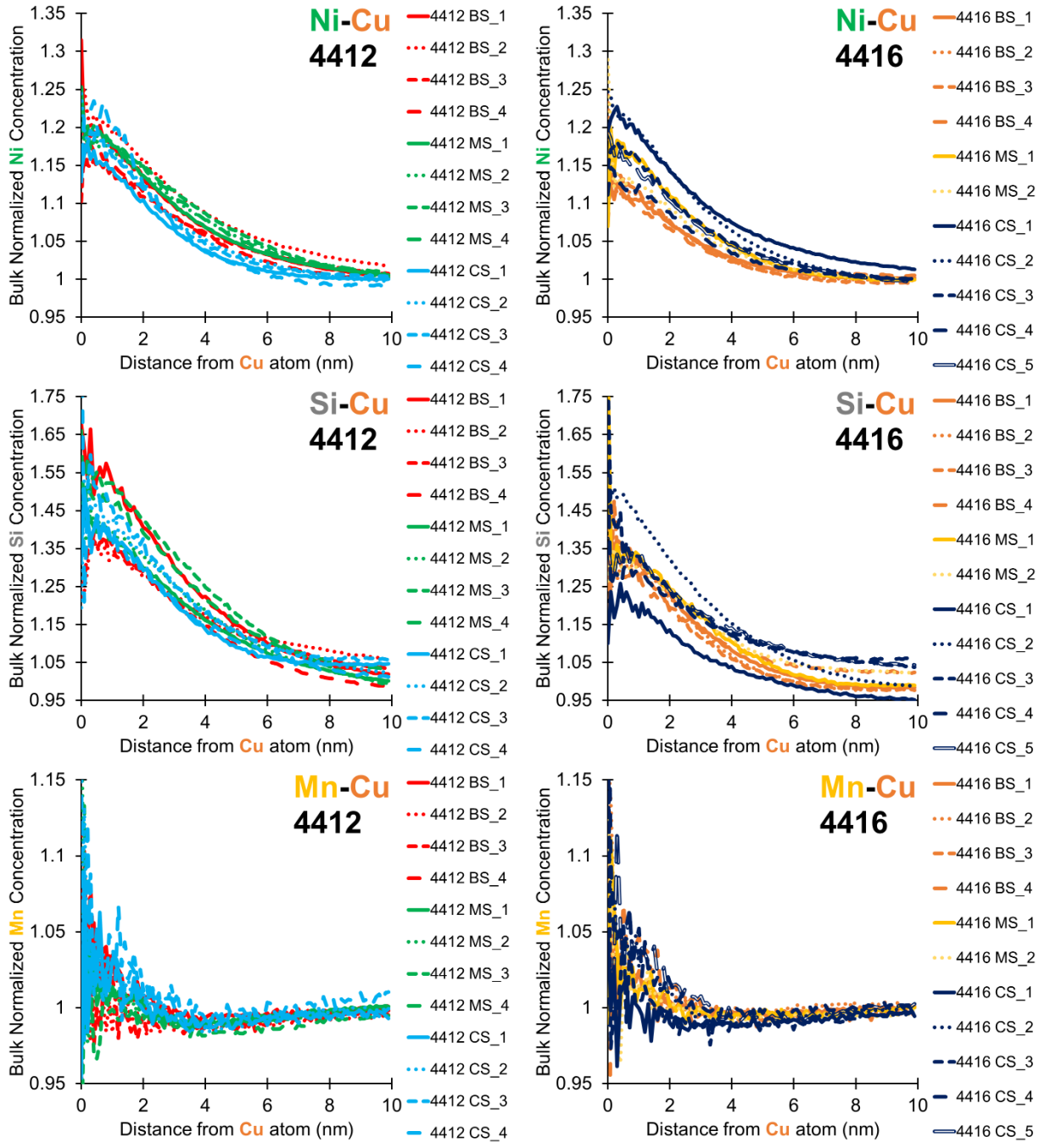
Ni-Cu
4412
Bulk Normalized Ni Concentration
Distance from Cu atom (nm)
4412 BS_1
4412 BS_2
4412 BS_3
4412 BS_4
4412 MS_1
4412 MS_2
4412 MS_3
4412 MS_4
4412 CS_1
4412 CS_2
4412 CS_3
4412 CS_4
Ni-Cu
4416
Bulk Normalized Ni Concentration
Distance from Cu atom (nm)
4416 BS_1
4416 BS_2
4416 BS_3
4416 BS_4
4416 MS_1
4416 MS_2
4416 CS_1
4416 CS_2
4416 CS_3
4416 CS_4
4416 CS_5
Si-Cu
4412
Bulk Normalized Si Concentration
Distance from Cu atom (nm)
4412 BS_1
4412 BS_2
4412 BS_3
4412 BS_4
4412 MS_1
4412 MS_2
4412 MS_3
4412 MS_4
4412 CS_1
4412 CS_2
4412 CS_3
4412 CS_4
Si-Cu
4416
Bulk Normalized Si Concentration
Distance from Cu atom (nm)
4416 BS_1
4416 BS_2
4416 BS_3
4416 BS_4
4416 MS_1
4416 MS_2
4416 CS_1
4416 CS_2
4416 CS_3
4416 CS_4
4416 CS_5
Mn-Cu
4412
Bulk Normalized Mn Concentration
Distance from Cu atom (nm)
4412 BS_1
4412 BS_2
4412 BS_3
4412 BS_4
4412 MS_1
4412 MS_2
4412 MS_3
4412 MS_4
4412 CS_1
4412 CS_2
4412 CS_3
4412 CS_4
Mn-Cu
4416
Bulk Normalized Mn Concentration
Distance from Cu atom (nm)
4416 BS_1
4416 BS_2
4416 BS_3
4416 BS_4
4416 MS_1
4416 MS_2
4416 CS_1
4416 CS_2
4416 CS_3
4416 CS_4
4416 CS_5

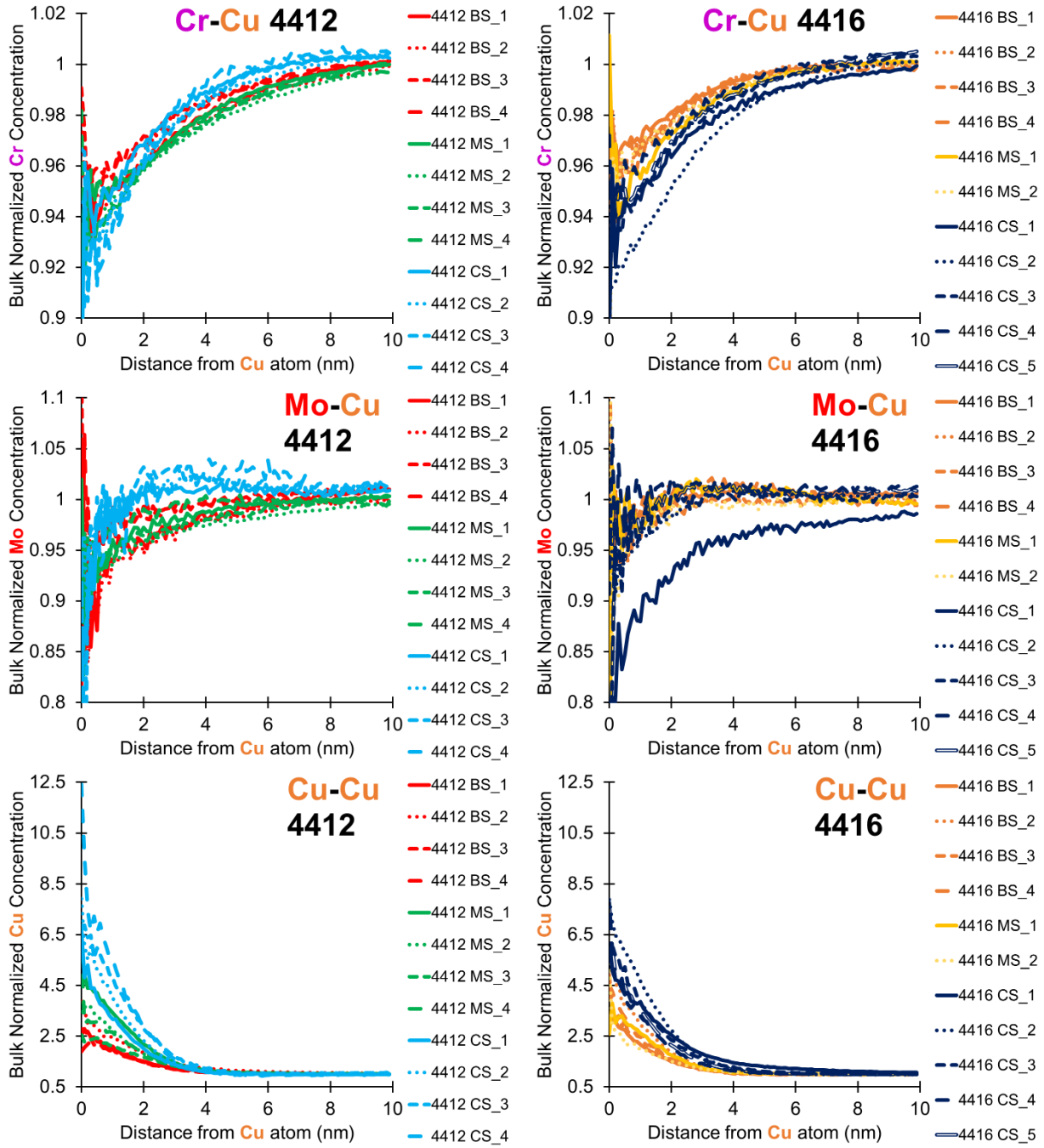

***Figure 3.8**: Bulk normalized Ni, Si, Mn, Cr, Mo, and Cu concentrations as a function of distance from a generic Cu atom for each of reconstructions for each section of BFB #4412 on the left and BFB #4416 on the right (marked as _1, _2, _3, _4, and _5, respectively), based on doing RDF analysis.*

3.2 Initial SEM-EBSD/EDS Characterization of IASCC cracking

Part of the collar slice or bolt head/shank intersection region was exposed to the primary water coolant in the two-loop downflow Westinghouse PWR [5]. Initial characterization of this region has started, first on the high dose bolt #4412. The CS slice in this bolt still had the exposed surface retained without excessive handling or processing damage. SEM analysis, as shown in Figure 3.9, demonstrated multiple small cracks along the specimen edge; all observed cracks were located inside the curved area, where stress would be

highest. The longest crack reached ~6 µm. SEM-EBSD and EDS analysis was performed to begin the investigation of these microcracks, as shown for one crack in Figure 3.10. According to EBSD data, the corrosion crack readily propagated along random high-angle grain boundaries (RHAB) and actually splits into two different directions at a triple junction of RHABs. Special boundaries such as low-angle grain boundaries (LAGB) or twin boundaries (sigma-3 [Σ3]) appear to be immune from cracking as seen in Figure 3.10(a), where the crack deflects and only travels along the RHAB despite hitting a triple junction of RHAB hitting a RHAB and a Σ3 boundary. Cracks propagated in the direction, normal to the surface suggesting the stress corrosion nature of this particular crack. According to the EDS data in Figure 3.10(b), the cracks may be filled with a Cr-rich oxide with Mo and Mn enriched at the sample surface in the region of the crack. It is unknown at this time if the crack formed first or if the oxide formed first.

These results are just the initial characterization, as the curved region of BFB #4416 is also planned to be investigated. The nature of these cracks is of interest as they were not observed by non-destructive testing and inspection when they were first removed from the plant. Also, it is of note that the torque required to remove the bolts was less than when first installed, suggesting there was some stress relief and perhaps arresting of the crack growth. More in depth characterization is required to understand the IASCC effects and mechanisms in these bolts.

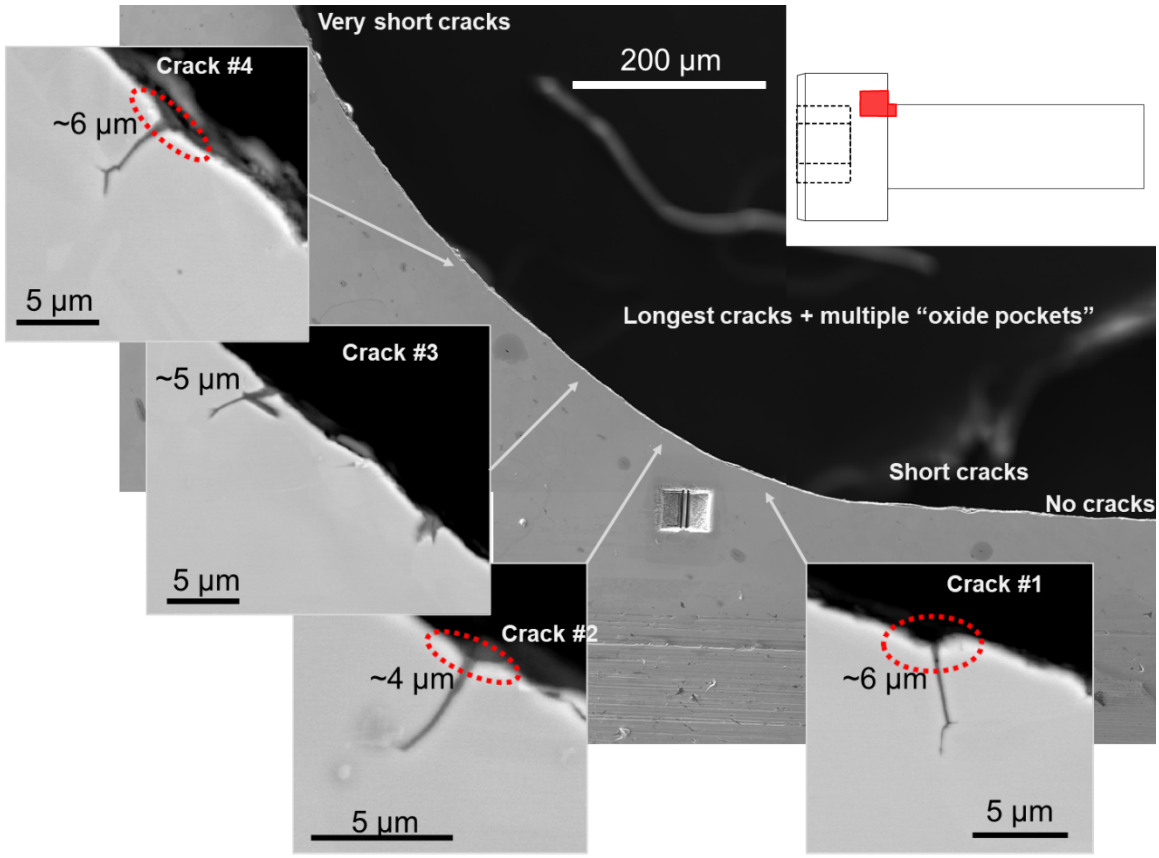

Figure 3.9*: SEM images from the curved section of BFB #4412 where the bolt head meets the bolt shank. Microscale cracks indicative of IASCC are found in the curved region and not in the straight regions.*

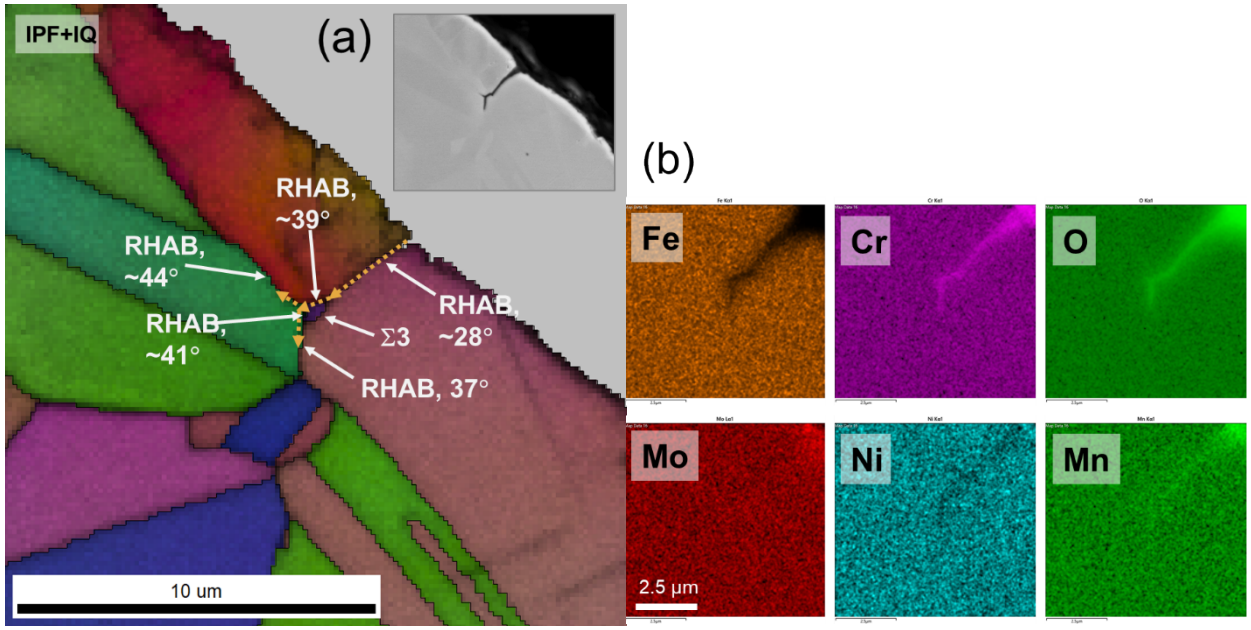

***Figure 3.10**: (a) SEM-EBSD inverse pole figure and image quality map of "crack #4" from Figure 3.9. (b) SEM-EDS maps showing the same crack filled with Cr, Mn, and O, and Mo segregated at the surface.*

4. CONCLUSIONS

In this report, we present our latest study in FY23 on microstructural characterization of both high fluence baffle-former bolts harvested from a commercial Westinghouse two-loop downflow type PWR using both APT and SEM. The objective of this project is to provide information that is integral to evaluating end of life microstructure and properties as a benchmark of international models developed for predicting radiation-induced swelling, segregation, precipitation, and mechanical property degradation. The main findings are summarized as follows:

1) Radiation-induced precipitation in the the two BFBs was highly complex, with the volume fraction and size of Ni/Si and Cu-rich precipitates depending strongly on the radiation temperature/dose. Unlike what seen by STEM-EDS, multi-phase precipitates were identified using APT, in which co-precipitates of adjoined clusters were found with Ni/Si-rich precipitates sandwiched between Cu-rich clusters and Cr/Mo/P-rich clusters. Ni/Si-rich clusters had a higher volume fraction in the thread sections of the bolt compared to the bolt head section, while the reverse was true for Cu-rich clusters. Comparing the two bolts, clustering was essentially the same for both bolts in the CS or bolt head section, but Ni/Si clustering was much higher in the BS or both thread section in the high dose bolt #4412 than in the lower dose bolt #4416.
2) Solute segregation out of solution was highest for most solute elements in the thread section of both bolts with the exception of Cu, which experienced more separation out of solution into Cu-rich clusters in the bolt head section. Solute segregation of each element out of solution was also more pronounced in the higher dose bolt #4412 than in the lower dose bolt #4416 in the BS and MS sections. This highlights the difference in the mechanisms for precipitation of Ni/Si clusters and precipitation of Cu-rich clusters. The immiscibility of Cu in FCC Fe favors lower temperature phase separation, while competition between ballistic mixing and thermal phase separation is more apparent for Ni/Si.
3) The lack of much change in solute segregation out of solution in the head section between the two bolts suggests that a steady-state for structural evolution has been reached in the CS section by the

dose in the CS section of the lower dose bolt #4416. Gradients in temperature, strain, and neutron energy spectrum likely affect the microstructural variation along the length of the bolt that overcomes the ~2X difference in irradiation dose that between the bolt head and the bolt thread. These gradients not only affect the steady-state size and distribution of precipitates but also the kinetics of when the steady-state is reached. The lower temperature of the CS section of the BFB reaches its steady-state sooner than the higher temperature of the MS and BS sections, which also have larger precipitate sizes.

4) Initial SEM characterization of the intersection of the bolt head with the bolt shank of the higher dose bolt #4412 where the bolt was exposed to primary coolant water reveals microcracks formed only in regions where there was additional stress due to the curvature of the bolt suggesting that IASCC is a cause for these cracks. The cracks observed are short – up to ~6 μm long – and only travel along high angle grain boundaries. It is uncertain why these cracks have not grown larger.

5. REFERENCES

[1] Stress Corrosion Cracking in Light Water Reactors: Good Practices and Lessons Learned, INTERNATIONAL ATOMIC ENERGY AGENCY, Vienna, 2011. https://www.iaea.org/publications/8671/stress-corrosion-cracking-in-light-water-reactors-good-practices-and-lessons-learned.

[2] X. (Frank) Chen, T. Chen, C.M. Parish, T. Graening, M.A. Sokolov, K.J. Leonard, Post-Irradiation Examination of High Fluence Baffle-Former Bolts Retrieved from a Westinghouse Two-Loop Downflow Type PWR, ORNL/TM-2019/1251, United States, 2019. https://doi.org/10.2172/1557483.

[3] T.G. Lach, X. (Frank) Chen, T.M. Rosseel, Microstructural characterization of the second high fluence baffle-former bolt retrieved from a Westinghouse two-loop downflow type PWR, ORNL/TM-2022/2668, 2022. https://doi.org/10.2172/1897832.

[4] X. (Frank) Chen, M.A. Sokolov, Fracture Toughness and Fatigue Crack Growth Rate Testing of Baffle-Former Bolts Harvested from a Westinghouse Two-Loop Downflow Type PWR, ORNL/TM-2021/2264, 2021.

[5] M.R. Ickes, J. McKinley, J.-K. Lee, J.M. Smith, A.M. Ruminski, M.A. Burke, Irradiation-assisted stress corrosion cracking of Type 347 and Type 316 steels irradiated in commercial pressurized water reactors, J. Nucl. Mater. 536 (2020) 152182. https://doi.org/10.1016/j.jnucmat.2020.152182.

[6] X. (Frank) Chen, K.J. Leonard, M.A. Sokolov, M.A. Burke, M.N. Gussev, S.R. Clark, Specimen Fabrication from Two High Fluence Ginna Baffle Bolts, ORNL/TM-2017/455, 2017.

[7] O.K. Chopra, A.S. Rao, Degradation of LWR Core Internal Materials due to Neutron Irradiation, NUREG/CR-7027, 2010.

[8] H.T. Tang, Materials Reliability Program Determination of Operating Parameters of Extracted Bolts (MRP-52), report number 1003076, EPRI technical report, 2001.

[9] D.J. Edwards, E.P. Simonen, F.A. Garner, L.R. Greenwood, B.M. Oliver, S.M. Bruemmer, Influence of irradiation temperature and dose gradients on the microstructural evolution in neutron-irradiated 316SS, J. Nucl. Mater. 317 (2003) 32–45. https://doi.org/10.1016/S0022-3115(03)00003-5.

[10] K.J. Leonard, M.A. Sokolov, M.N. Gussev, Post-Service Examination of PWR Baffle Bolts, Part I. Examination and Test Plan, Oak Ridge National Laboratory Report, ORNL/LTR-2015/193, 2015.

[11] A. Devaraj, D.E. Perea, J. Liu, L.M. Gordon, T.J. Prosa, P. Parikh, D.R. Diercks, S. Meher, R.P. Kolli, Y.S. Meng, S. Thevuthasan, Three-dimensional nanoscale characterisation of materials by atom probe tomography, Int. Mater. Rev. 63 (2018) 68–101. https://doi.org/10.1080/09506608.2016.1270728.

[12] A. Devaraj, T.C. Kaspar, S. Ramanan, S. Walvekar, M.E. Bowden, V. Shutthanandan, R.J. Kurtz, Nanoscale phase separation in epitaxial Cr-Mo and Cr-V alloy thin films studied using atom probe

tomography: Comparison of experiments and simulation, J. Appl. Phys. 116 (2014) 193512. https://doi.org/10.1063/1.4901465.
[13] J. Zhou, J. Odqvist, M. Thuvander, P. Hedström, Quantitative Evaluation of Spinodal Decomposition in Fe-Cr by Atom Probe Tomography and Radial Distribution Function Analysis, Microsc. Microanal. 19 (2013) 665–675. https://doi.org/10.1017/S1431927613000470.
[14] O.C. Hellman, J.A. Vandenbroucke, J. Rüsing, D. Isheim, D.N. Seidman, Analysis of Three-dimensional Atom-probe Data by the Proximity Histogram, Microsc. Microanal. 6 (2000) 437–444. https://doi.org/10.1007/S100050010051.
[15] T.G. Lach, D.A. Collins, T.S. Byun, Evolution of the role of molybdenum in duplex stainless steels during thermal aging: From enhancing spinodal decomposition to forming heterogeneous precipitates, J. Nucl. Mater. 557 (2021) 153268. https://doi.org/10.1016/j.jnucmat.2021.153268.
[16] T.G. Lach, W.E. Frazier, J. Wang, A. Devaraj, T.S. Byun, Precipitation-site competition in duplex stainless steels: Cu clusters vs spinodal decomposition interfaces as nucleation sites during thermal aging, Acta Mater. 196 (2020) 456–469. https://doi.org/10.1016/j.actamat.2020.05.017.
[17] R.A. Enrique, P. Bellon, Compositional Patterning in Systems Driven by Competing Dynamics Of Different Length Scale, Phys. Rev. Lett. 84 (2000) 2885–2888. https://doi.org/10.1103/PhysRevLett.84.2885.
[18] N. Almirall, P.B. Wells, S. Pal, P.D. Edmondson, T. Yamamoto, K. Murakami, G.R. Odette, The mechanistic implications of the high temperature, long time thermal stability of nanoscale Mn-Ni-Si precipitates in irradiated reactor pressure vessel steels, Scr. Mater. 181 (2020) 134–139. https://doi.org/10.1016/j.scriptamat.2020.02.027.
[19] M. Mamivand, P. Wells, H. Ke, S. Shu, G.R. Odette, D. Morgan, CuMnNiSi precipitate evolution in irradiated reactor pressure vessel steels: Integrated Cluster Dynamics and experiments, Acta Mater. 180 (2019) 199–217. https://doi.org/10.1016/j.actamat.2019.09.016.
[20] Y. Huang, J.M.K. Wiezorek, F.A. Garner, P.D. Freyer, T. Okita, M. Sagisaka, Y. Isobe, T.R. Allen, Microstructural characterization and density change of 304 stainless steel reflector blocks after long-term irradiation in EBR-II, J. Nucl. Mater. 465 (2015) 516–530. https://doi.org/10.1016/j.jnucmat.2015.06.031.